Journal of Geophysical Research, Vol. 105, No. A9, Pages 20,833-20,856, September 1, 2000.

The thermosphere of Titan simulated by a global three-dimensional time-dependent model

I. C. F. Müller-Wodarg,[1,2] R. V. Yelle,[2,3] M. Mendillo,[2] L. A. Young,[2,4]
and A. D. Aylward[1]

Abstract

We present three-dimensional numerical simulations for dynamics and energetics of Titan's thermosphere. In so doing, we distinguish between the dynamics driven by solar insolation and those driven by vertical coupling to winds in Titan's middle atmosphere. Our calculations reveal that the solar-driven thermospheric dynamics are characterized by the balance between pressure gradients and viscosity, while the super-rotating zonal winds detected in Titan's stratosphere set up a balance between the pressure gradients, curvature and Coriolis forces. The day to night temperature gradients in the upper thermosphere (around 1300 km) typically lie around 20 (10) K for solar maximum (minimum), with peak solar-driven winds of around 60 (30) m/s. This difference decreases with height and virtually disappears below 1000 km as a result of dayside adiabatic cooling and nightside adiabatic heating. The model highlights unique features about the thermosphere on Titan, such as the important nighttime heating from mid-latitudes to high-latitudes caused by the relatively small size of the planet's shadow, leading to features in the wind profiles which are not found on Earth. Although the lack of measurement constraints prevents us from making predictions of actual wind profiles on Titan, the model does illustrate the physical processes driving the dynamics and suggests that anticipated thermospheric measurements from the Cassini spacecraft may provide constraints also for the dynamics at lower altitudes.

1. Introduction

Titan is the largest moon of Saturn, with a radius of around 2575 km and a gravity strong enough to hold a permanent atmosphere. In many respects the atmosphere of Titan resembles that of Earth. In terms of vertical thermal structure, both may be subdivided into the same regions, a troposphere, stratosphere, mesosphere and thermosphere. This paper is concerned with Titan's thermosphere only and thus investigates behavior of the neutral constituents in Titan's upper atmosphere. On both planets the thermosphere begins near the 1 bar pressure level, corresponding to around 80 km altitude on Earth and 600 km on Titan. In terms of composition the thermospheres also have some similarities, with N_2 being a major constituent. Other key components in Titan's thermosphere are hydrocarbons such as CH_4, C_2H_2, and HCN, while the terrestrial thermosphere has a strong abundance of O and O_2.

We know little about the global thermospheric dynamics on Titan and report here on the first application of a general circulation model (GCM) to the thermosphere of Titan. Our goal in this paper is primarily elucidation of the basic dynamical state of the upper atmosphere, rather than the detailed prediction of realistic winds fields. We estimate the magnitude of local time and latitudinal temperature differences, the winds driven by these temperature variations, and their effect on the thermal structure. Through analysis of the calculations we attempt to determine the dominant terms in the energy and momentum equations and thereby arrive at an understanding of the basic balances that govern the upper atmosphere of Titan. In doing so we will distinguish between thermospheric dynamics generated in situ by solar heating and those generated by dynamical coupling to lower altitudes.

General circulation models (GCMs) are a powerful tool with which to study planetary upper atmospheres. They can be used to investigate basic physical processes, to provide a context for more specific investigations, and to make predictions useful for planning observational investigations. Study of the Earth's thermosphere with GCMs [*Roble et al.,* 1988; *Fuller-Rowell et al.,* 1996] has led to identification of the basic sources and sinks of energy as well as the forces that drive the dynamics of the upper atmosphere. Much of the current research on the terrestrial thermosphere focuses on the interaction between the thermosphere, ionosphere, and magnetosphere, such as the response to geomagnetic storms [*Fuller-Rowell et al.,* 1994; *Burns et al.,* 1995]. Application of GCMs to Venus indicates that solar heating, cooling by CO_2 emissions and thermal conduction determine thermal structure, but these investigations have been forced to adopt an empirical viscosity (thought to represent wave drag) to accurately model observed wind speeds [*Bougher and Roble,* 1991; *Bougher et al.* 1999]. Investigation of the Martian thermosphere with GCMs suffers from a lack of observational constraints, but the modeling work suggest that absorption of sunlight by aerosols may be an important energy source, in addition to the processes identified on Earth and Venus [*Bougher et al.,* 1988; 1990; 1993; 1997; 1999]. GCMs for Jupiter have only recently been constructed [*Achilleos et al.* 1998] in an attempt to explain observed global temperature distributions and the transport of energy from auroral regions to mid and low latitudes.

Most of our current knowledge about Titan was obtained from remote sensing experiments during the Voyager 1 and 2 flybys in November 1980 and August 1981, respectively. The thermal structure of Titan's atmosphere below 200 km was measured by the radio occultation experiment (RSS), infrared interferometer spectrometer (IRIS), and ultraviolet spectrometer (UVS) of Voyager 1 on November 12, 1980 [*Lindal et al.,* 1983; *Lellouch et al.,* 1989; *Yelle et al.,* 1997], while the thermal structure above 500 km was derived both from the ultraviolet solar occultation experiment of UVS [*Smith et al.,* 1982] and the IRIS measurements on Voyager 2 on August 27, 1981 [*Letourner and Coustenis,* 1993]. The occultation of 28 Sgr by Titan in July 1989 provided additional important information, allowing the derivation of temperature, pressure, haze optical depth and zonal velocities as a function of latitude and altitude in the 250 to 450 km height regime [*Hubbard et al.,* 1993]. The described measurements where made over the past 20 years, thus spanning almost the duration of one Titan year (29.46 Earth years). It is thus important to compare the seasons for each measurement. Figure 1 shows Titan's subsolar latitudes from years 1975 to 2010, with seasons, the times of important past and future observations, as well as the years of solar maximum and minimum conditions labeled. We see from Figure 1 that Voyager measurements were made close to equinox on Titan at solar maximum, while the Cassini spacecraft will, over its anticipated lifetime of around 4 years between December 2004 and December 2008, encounter late Southern Hemisphere

Figur

summer to spring conditions at low to medium solar activity level. Figure 1 also illustrates that one Titan year extends over more than two complete solar cycles, in contrast to the situation on Earth. This may have important implications on the seasonal behavior on Titan, which, however, is beyond the scope of this paper.

The work presented here has been motivated by the Cassini mission and the potential it offers for detailed and comprehensive measurements of Titan's upper atmosphere. Our results may be useful for Cassini mission planning in the sense that we identify interesting areas for observational investigations and estimate basic parameters, such as scale lengths for temperature variations and orders of magnitude of wind speeds, amongst other parameters.

Basic issues concerning the dynamics of Titan's thermosphere have previously been discussed by *Rishbeth et al.* [2000]. Using scale analysis of the equations of motion, Rishbeth et al. argue that the dynamics of Titan's upper atmosphere differs from that of the Earth in some fundamental ways. The lack of a strong magnetic field on Titan implies that ion drag, an important force on the Earth, is absent on Titan. Moreover, the slower rotational velocity implies that Coriolis forces are reduced. However, potentially large wind speeds imply that curvature terms in the equation of motion could be large. Molecular viscosity forces, according to Rishbeth et al., tend to be weaker on Titan than on Earth, as a consequence of the lower temperature. The coefficient of dynamic viscosity varies with temperature (T) as $T^{0.75}$; moreover, the density at a given pressure level is much higher on Titan than on Earth because of the lower temperature, reducing the effects of viscosity even further. In essence, then, as suggested by Rishbeth et al., the dynamics of Titan's upper atmosphere is simpler than for Earth. The basic balance is between pressure gradients created by variations of solar energy deposition and inertial terms that arise because motions are confined to the surface of a sphere. We will discuss how these results compare to those obtained with the three-dimensional numerical modeling (see section 4.2).

Some aspects of Titan's thermospheric dynamics are difficult to estimate with the scale analysis employed by *Rishbeth et al.* [2000], particularly the influence of adiabatic heating on the temperature profile. First results on that question are presented here in section 4. We find that vertical winds greatly affect the temperature profile in Titan's thermosphere. They operate to cool the dayside and heat the nightside. The efficiency of this process is primarily a consequence of the extended nature of the atmosphere. The thermosphere of Titan occupies a region of 800 km altitude. This is about 16% the radius of its thermosphere, whereas the Earth's thermosphere has a vertical extent only 6% of its radius. Ultimately, this is a consequence of the small size of the moon as compared to the Jovian or terrestrial planets. Vertical gradients of gravity acceleration are larger on Titan than on the Jovian or terrestrial planets, so the dayside (nightside) atmospheric expansion (contraction) is enhanced by the gases reaching to higher (lower) altitudes where gravity is smaller (larger). As a result, the adiabatic heating and cooling processes are more pronounced on Titan.

One-dimensional models for the thermal structure of Titan's upper atmosphere have been constructed by *Friedson and Yung* [1984], *Lellouch* [1990] and *Yelle* [1991]. All of these studies have been based on Voyager data, primarily the solar occultation experiment observed with the ultraviolet spectrometer. In their analysis of these data, *Smith et al.* [1982] determined an exospheric temperature of 185±20 K, a CH_4 mole fraction of $8 \pm 3\%$ and a C_2H_2 mole fraction of around 1%. This pioneering investigation represented the first direct measurement of the composition of Titan's atmosphere and, along with the results from the radio occultation [*Lindal et al.,* 1983] and infrared observations [*Hanel et al.,* 1981], the first direct measurement of the temperature of Titan's atmosphere. Subsequently, *Strobel et al.,* [1992] pointed out apparent inconsistencies in the determination of CH_4 densities by Smith et al. and suggested a significantly lower mole fraction. A comprehensive analysis by R. J. Vervack et al. (First results from a reanalysis of the Voyager 1 ultraviolet spectrometer solar occultation by Titan, submitted to *Icarus,* 2000) (hereinafter referred to as (Vervack et al., submitted manuscript, 2000)) finds CH_4 and C_2H_2 mole fractions smaller than the results by Smith et al. and an exospheric temperature of 150 ± 3 K, nearly 25 K cooler. The results presented here were completed prior to distribution of the analysis by Vervack et al. and continue to be based on results by *Smith et al.* [1982]. We believe that this is the wisest course, since it maintains consistency with previous work on Titan's upper atmosphere. Moreover, experiments with our GCM have shown that the dynamics described in the following are largely unaffected by the exact exospheric temperature values in Titan's thermosphere. Our exospheric

temperature can be influenced externally by changing composition, which influences the solar heating and radiative cooling, and by varying the lower boundary (600 km altitude) temperature. In principle, therefore, we should obtain the exospheric temperatures by Vervack et al. (submitted manuscript, 2000) by simply changing our constituent mixing ratios and lower boundary temperatures value to fit theirs.

In section 2 we describe the Titan GCM in detail. Sections 3 focuses on the comparison between globally averaged energetics calculated by one-dimensional and 3-D codes, while section 4 presents and discusses results from 3-D calculations of thermospheric winds and temperatures forced in situ by solar heating. Section 5 investigates the role of dynamical forcing from the lower atmosphere, compared with that deriving from solar heating alone.

2. The Model

2.1. Approach

Our calculations encompass the atmosphere from 600 to 1400 km (0.147 to $0.9 \times 10^{-6}\mu$ bar). In the 1-D models of *Yelle* [1991], 600 km represents the approximate location of the mesopause. This represents a convenient boundary because there is little thermal conduction through the mesopause and it represents a minimum in the solar heating rate. Above the mesopause the atmosphere is heated by solar EUV and Lyman α radiation; below the mesopause the atmosphere is heated by longer wavelength solar UV radiation and solar IR radiation. Also, radiative heating in the vibrational bands of hydrocarbons becomes progressively more important at lower altitudes [*Yelle,* 1991]. Inclusion of these processes would be complex and prohibitively time consuming.

The only energy source included in our calculations is heating through the absorption of sunlight. We are aware of the possibility that significant amounts of energy are deposited by charged particles from the magnetosphere. However, magnetospheric precipitation on Titan is still poorly understood. Estimates that have been performed suggest energy fluxes comparable to the solar energy flux, but with a different spatial distribution [*Galand et al.,* 1999]. If this is correct then Titan's magnetospheric interaction may alter the direction of the thermospheric winds and location and size of temperature gradients but it should not alter the balance of forces, our primary focus in this paper. For this reason we have chosen to model only the simple, solar-driven case. Energy input from the magnetosphere will be included in future applications of this model.

Given the similarities between the terrestrial and Titan's thermospheres, our approach was to adapt an existing terrestrial model, the University College London Thermosphere Model, which is the thermospheric component of the Coupled Thermosphere-Ionosphere Model (CTIM) by *Fuller-Rowell et al.* [1996], to Titan. Although this is a common procedure when developing planetary models, due to the relatively extensive availability of Earth models, this method generally needs to be used with caution: a number of approximations are frequently made for Earth which cannot be used on Titan or other small planets. While much of the program structure is taken from the CTIM code, some key components, such as the solar heating and radiative cooling algorithms, were specifically rewritten for Titan and are described in sections 2.4 and 2.5, respectively.

2.2. Fundamental Equations

The coordinate system used is a Eulerian spherical corotating pressure grid, with horizontal coordinates being latitude and longitude. The three- dimensional momentum equation in Titan's thermosphere is given by

$$\frac{d\vec{U}}{dt} = \vec{g} - \frac{1}{\rho}\vec{\nabla}p - 2\vec{\Omega} \times \vec{U} + \frac{1}{\rho}\vec{\nabla}(\mu\vec{\nabla}\vec{U}), \qquad (1)$$

where $\vec{U}$ denotes the three-dimensional velocity vector and $\vec{\nabla}$ the three-dimensional differential operator, $\vec{g}$ is gravity acceleration, ρ the mass density, p the pressure, $\vec{\Omega}$ is Titan's rotation vector (with $\Omega = 4.6 \times 10^{-6} s^{-1}$, corresponding to 15.8 Earth days) and μ is the coefficient of viscosity. Since Titan's rotation period is identical to its orbital period around Saturn, the same side of Titan always faces the planet. Note that (1) is given in its general form on a height coordinate system, as seen from the presence of the explicit pressure gradient term (second term on the right side), while in the following we will be using all fundamental equations in the pressure coordinate frame. The time derivative of the velocity vector $\vec{U}$ in spherical coordinates is more complex than for a Cartesian vector since the unit vectors $\vec{\imath}$, $\vec{\jmath}$, and $\vec{k}$ in the latitudinal, longitudinal, and vertical directions, respectively, are not constant with time. Differentiating the unit vectors with time thus yields additional terms, and the total derivative of $\vec{U}$ with time becomes

$$\begin{aligned}\frac{d\vec{U}}{dt} &= \left(\frac{du_\theta}{dt} - \frac{u_\varphi^2}{a\cdot tan\theta} + \frac{wu_\theta}{a}\right)\vec{i} \\ &+ \left(\frac{du_\varphi}{dt} + \frac{u_\varphi u_\theta}{a\cdot tan\theta} + \frac{wu_\varphi}{a}\right)\vec{j} \\ &+ \left(\frac{dw}{dt} - \frac{u_\theta^2+u_\varphi^2}{a}\right)\vec{k}.\end{aligned} \quad (2)$$

Here u_θ, u_φ and w are the neutral wind components, defined as positive southward, eastward, and upward, respectively; a is the distance of the current position to the center of the planet, θ is colatitude and t is time. Note that w is the vertical wind in the pressure frame, defined as $w = dp/dt$, where p is pressure. The total time derivatives of scalars on the right side of equation (2) can further be expanded into

$$\frac{d}{dt} = \frac{\partial}{\partial t} + u_\theta\frac{1}{a}\frac{\partial}{\partial\theta} + u_\varphi\frac{1}{a\cdot sin\theta}\frac{\partial}{\partial\varphi} + w\frac{\partial}{\partial p}, \quad (3)$$

where φ denotes the longitude. The other terms in the brackets of (2) are often referred to as the curvature terms. They represent the centrifugal force experienced by gas particles as they move along a curved surface. In the model we explicitly solve only the horizontal components of the momentum equation which by combining (1), (2), (3) and the hydrostatic equation as well as applying the spherical differential operators $\vec{\nabla}$ and $\vec{\nabla}^2$ become

$$\begin{aligned}\frac{\partial u_\theta}{\partial t} =& -\left(u_\theta\frac{1}{a}\frac{\partial u_\theta}{\partial\theta} + u_\varphi\frac{1}{a\cdot sin\theta}\frac{\partial u_\theta}{\partial\varphi} + w\frac{\partial u_\theta}{\partial p}\right) \\ &+ \left(\frac{-wu_\theta}{a} + \frac{u_\varphi^2}{a\cdot tan\theta}\right) - \frac{g}{a}\frac{\partial h_p}{\partial\theta} \\ &+ 2\Omega u_\varphi cos\theta \\ &+ \frac{1}{\rho}\left(\vec{\nabla}_p^2 u_\theta + \frac{1}{a^2}\frac{\partial\mu}{\partial\theta}\frac{\partial v_\theta}{\partial\theta} + \frac{1}{a^2 sin^2\theta}\frac{\partial\mu}{\partial\varphi}\frac{\partial v_\theta}{\partial\varphi}\right) \\ &+ g\frac{\partial}{\partial p}\left(\mu\rho g\frac{\partial v_\theta}{\partial p}\right),\end{aligned} \quad (4)$$

$$\begin{aligned}\frac{\partial u_\varphi}{\partial t} =& -\left(u_\theta\frac{1}{a}\frac{\partial u_\varphi}{\partial\theta} + u_\varphi\frac{1}{a\cdot sin\theta}\frac{\partial u_\varphi}{\partial\varphi} + w\frac{\partial u_\varphi}{\partial p}\right) \\ &- \left(\frac{wu_\varphi}{a} + \frac{u_\theta u_\varphi}{a\cdot tan\theta}\right) - \frac{g}{a\cdot sin\theta}\frac{\partial h_p}{\partial\varphi} \\ &- 2\Omega u_\theta cos\theta \\ &+ \frac{1}{\rho}\left(\vec{\nabla}_p^2 u_\varphi + \frac{1}{a^2}\frac{\partial\mu}{\partial\theta}\frac{\partial v_\varphi}{\partial\theta} + \frac{1}{a^2 sin^2\theta}\frac{\partial\mu}{\partial\varphi}\frac{\partial v_\varphi}{\partial\varphi}\right) \\ &+ g\frac{\partial}{\partial p}\left(\mu\rho g\frac{\partial v_\varphi}{\partial p}\right).\end{aligned} \quad (5)$$

Here $\vec{\nabla}_p$ is the two-dimensional gradient operator on a level of fixed pressure. For its square we use the expression

$$\vec{\nabla}_p^2 = \frac{1}{a^2}\frac{\partial^2}{\partial\theta^2} + \frac{cos\theta}{a^2 sin\theta}\frac{\partial}{\partial\theta} + \frac{1}{a^2 sin^2\theta}\frac{\partial^2}{\partial\varphi^2}. \quad (6)$$

The assumption of hydrostatic balance implies that vertical accelerations are considered to be small in relation to gravity. The forces acting upon a gas particle are given on the right sides of (4) and (5) as advection, curvature forces, pressure gradient, Coriolis force, horizontal, and vertical viscosity. Advection physically represents the horizontal and vertical transport of momentum by winds, while the curvature terms, as mentioned earlier, are a result of the spherical geometry (see (2)). The pressure gradient is expressed as a gradient in the height of the pressure level h_p, assuming hydrostatic balance. The viscosity tends to act opposite to the pressure gradient and thus represents a damping force, attempting to remove gradients in the three- dimensional velocity field. The momentum equation (1) contains no ion-neutral coupling term. Although Titan has an ionosphere [*Bird et al.* 1997], the effect of the ionosphere on dynamics is likely to be nil because of the low ion densities and weak geomagnetic field on Titan [*Rishbeth et al.,* 2000] and is therefore not considered here. Due to the presence of Saturn's magnetic field at higher altitudes (above 1500 km), the ion-neutral coupling may become more important there, but is beyond the scope of this study.

In the vertical direction, the pressure gradient and gravity acceleration dominate other terms by several orders of magnitude and an accurate numerical calculation of the vertical velocity w is not possible on the basis of (1). Vertical winds are therefore calculated using the continuity equation which in the pressure coordinate system reduces to the simple form of

$$\frac{1}{a \cdot sin\theta} \frac{\partial}{\partial \theta} u_\theta \, sin\theta + \frac{1}{a \cdot sin\theta} \frac{\partial u_\varphi}{\partial \varphi} + \frac{\partial w}{\partial p} = 0. \quad (7)$$

Physically, the equation expresses that any divergence in the horizontal velocity field must be balanced by vertical wind in order to conserve mass.

The energy balance for any gas is given by the sum of the internal and external energy sources and sinks. In a spherical pressure coordinate system this balance may be expressed by the relation

$$\begin{aligned} &\frac{\partial \epsilon}{\partial t} + \vec{V}_p \, \vec{\nabla}_p \, (\epsilon + g h_p) + w \, \frac{\partial (\epsilon + g h_p)}{\partial p} \\ &\quad = Q_{EUV} + Q_{IR} + g \frac{\partial}{\partial p} \left(\frac{(K_m + K_\tau)}{H} \, p \, \frac{\partial T}{\partial p} \right) \\ &\quad + \frac{1}{\rho} (K_m + K_\tau) \, \vec{\nabla}_p^2 T \qquad (8) \\ &\quad + g \frac{\partial}{\partial p} \, (u_\theta \mu \frac{\partial u_\theta}{\partial p} + u_\varphi \mu \frac{\partial u_\varphi}{\partial p}). \end{aligned}$$

Here ϵ is the sum of internal and kinetic energies per unit mass, defined as $\epsilon = c_p T + 0.5\,(u_\theta^2 + u_\varphi^2)$, g is the (height dependent) value of the gravity acceleration vector, h_p is again the height of the pressure level, and T is gas temperature. With $g h_p$ representing the potential energy of the gas at height h_p, the term $\epsilon + g h_p$ is thus its enthalpy. The principal external energy source in Titan's atmosphere Q_{EUV} is solar EUV and FUV radiation which is absorbed by N_2 and CH_4 at wavelengths primarily between 75 and around 1300 $\mathring{A}$ (see section 2.4). Radiative cooling Q_{IR} occurs in the rotational lines of HCN (see section 2.5). The other terms on the right side of (8) denote vertical and horizontal molecular and turbulent heat conduction as well as heating by viscosity. K_m and K_τ are the molecular and turbulent coefficients of heat conduction, respectively, of which the latter is set to zero in our model and the former is defined in section 2.3. On the left side of (8) the term $w \, \partial\epsilon/\partial p$ represents vertical transport of energy, while $w \, \partial(g h_p)/\partial p$ is the adiabatic heating and cooling term. In section 4 the relative importance of the various acceleration and energy flux terms will be discussed.

2.3. Parameters and Boundary Conditions

A number of external parameters are specified in the model, such as composition, solar fluxes, absorption cross sections for each constituent at every wavelength as well as coefficients of viscosity and heat conduction. We consider only three constituents, N_2, CH_4 and HCN. The relative abundance of these species, especially HCN, is not well known, so we do not attempt a self-consistent calculation of mole fractions but simply specify the values on every pressure level. At the same time, number densities do change as the atmosphere expands and contracts and are calculated from the pressure and temperature, using the ideal gas law. We use the mole fraction profiles calculated by *Yung et al.* [1984], but scale them slightly to achieve the desired exospheric temperature. This choice of molecular species is based on the fact that N_2 and CH_4 are the most abundant constituents and are important absorbers of solar energy. HCN, though far less abundant, is an important source of cooling, through rotational line emissions at far infrared wavelengths [*Yelle,* 1991]. Thus with N_2, CH_4, and HCN we can account for the primary sources of radiative heating and cooling in the thermosphere.

With N_2 being the main constituent in Titan's thermosphere in the height range of interest here, we use the expression by *Bauer* [1973] for nitrogen to calculate the molecular heat conduction coefficient: $K_m = 27.21 \times 10^{-5} \, T^{0.80}$ $(J/m/K/s)$, where T is the neutral gas temperature. Eddy heat conduction, as mentioned earlier, is set to zero in our calculations. The molecular viscosity coefficient has a value of $\mu = 1 \times 10^{-5} (kg/m/s)$ [*National Bureau of Standards,* 1959], which is based on measurements for the temperature range found in Titan's thermosphere (100-200 K). Experiments with the Titan GCM showed that results were not sensitive to variations of the molecular viscosity coefficient by 50% in either direction, even though discussions in section 4.2 will demonstrate the importance of molecular viscosity in Titan's thermosphere.

Additional boundary conditions used in the model are as follows: we assume zero second vertical derivatives in all parameters at the upper boundary, while default lower boundary conditions are zero winds and globally constant temperature, altitude and density. In section 5 we describe experiments in which the lower boundary altitude and winds are changed.

2.4. Solar Heating

Titan's extended atmosphere makes the global solar heating profile unique. The vertical extent of the thermosphere is around 800 km and implies that the shadow of the solid body is small relative to the size of its thermosphere. This is illustrated in Figure 2, where a latitude-height profile of thermospheric so-

Figur

lar heating rates is shown at a longitude "slice" from the subsolar to the antisolar point. The right side in Figure 2 thus represents the dayside and the left side represents the nightside. Radiation is extinguished on the nightside of Titan, not because it is intercepted by the surface, but because the path length through the atmosphere becomes long. Only a small region, deep on the nightside, is shielded by the surface. The transition from day to night is softer than in a less extended atmosphere and the polar regions are in continual sunlight. The lengthening of the day with increasing latitude partially offsets the decrease of solar insolation due to obliquity. Latitudinal gradients are less severe in Titan's thermosphere than in other thermospheres.

The solar heating calculations are performed by explicitly integrating the heating along the ray paths through Titan's atmosphere every few time steps. We assumed heating efficiencies of 0.5 for both N_2 and CH_4. Solar EUV fluxes between 75 and 1050 $\mathring{A}$ wavelength are obtained from *Torr and Torr* [1985], while FUV fluxes between 1050 and 1775 $\mathring{A}$ are taken from *London et al.* [1993]. The calculations reveal that the heating rate per unit volume is relatively constant from 700 to 1100 km with two slight maxima near 750 and 1000 km (solid curves in Figure 3; see also discussions in section 3.2). Heating by solar EUV dominates above 950 km and FUV (primarily Lyman α) below. Comparison of the total energy absorbed by the thermosphere with the integrated flux from the Sun indicates that Titan presents the solar EUV and FUV flux with an obstacle of roughly 3700 km radius, assuming a mean heating efficiency of 50%. This represents twice the area of the solid moon.

2.5. Radiative Cooling

We assume that above 600 km HCN is the only significant radiatively active molecule. Examination of Figure 15 in *Yelle* [1991] shows that cooling in mid-infrared vibrational bands of hydrocarbon molecules (CH_4, C_2H_2, C_2H_6) contributes at altitudes between 600 and 700 km. The radiative transfer in these bands is complex and time consuming to calculate and therefore difficult to incorporate into a GCM. The neglect of cooling in hydrocarbon vibrational bands introduces some uncertainty into the temperature structure near the lower boundary in our model; however, 1-D calculations with and without the hydrocarbon cooling indicate temperature differences of only a few degrees Kelvin. This is smaller than other uncertainties in the problem. Moreover, as these terms are constant in local time and their primary effect with latitude is to change the temperature in the stratosphere (our lower boundary), it seems unlikely that the hydrocarbon cooling will influence the dynamics of the thermosphere.

Cooling by HCN is a simpler problem because it arises from pure rotational lines, which are few in number and in local thermodynamic equilibrium (LTE). The radiative cooling rate at height z can be expressed as

$$Q_R(z) \;=\; 2\pi N_i \sum_l S_l \int_l \Phi_\nu(z) d\nu \cdot X(\nu, l, z), \quad (9)$$

where

$$\begin{aligned} X(\nu,l,z) \;&=\; B_\nu(0)E_z(\tau_\nu(0)-\tau_\nu(z)) - B_\nu(z) \\ &+\; \int_0^\infty N_i S_l(z') B_\nu(z') \\ &\quad \cdot E_1(\mid \tau_\nu(z)-\tau_\nu(z') \mid)\Phi_\nu(z')\cdot dz'. \end{aligned} \quad (10)$$

In these expressions l denotes a particular spectral line, S_l is the line strength, B_ν is the Planck function, τ_ν is the monochromatic optical depth measured vertically downward, Φ_ν represents the line shape function, E_1 is an exponential integral, and N_i is the HCN number density. We evaluate this expression by numerical integration over all relevant spectral lines. The line parameters are obtained from the 1996 edition of the HITRAN tape [*Rothman et al.,* 1992]. We assume pressure-broadened voigt line shapes and negligible overlap of spectral lines; this is well justified for the widely separated HCN lines at the low densities in Titan's upper atmosphere.

2.6. Model Implementation

To calculate the dynamics of Titan's thermosphere, we solve (4), (5), (7), and (8) on a grid of latitude, longitude, and pressure levels. In our simulations the grid has 6° increments in latitude and 18° increments in longitude, but the code is designed to also allow the use of any other resolution. The vertical coordinate is a level of constant pressure, given by an index n, which is related to the pressure by

$$p = p_0 \cdot e^{-\alpha(n-1)}. \quad (11)$$

Here $p_0 = 1.47 \times 10^{-2}\ (Pa) \;\; = 0.147\ (\mu bar)$ is the pressure at the lower boundary ($n = 1$) altitude of

600 km and α is the vertical resolution in fractions of one scale height, which can also be adjusted for each simulation. In all simulations presented here we chose $\alpha = 0.5$, implying a half scale height resolution, and let n run from 1 to 25, giving a height coverage from 600 km to around 1400 km. The top pressure level becomes, following (11), $p_{Top} = 0.9 \times 10^{-6}\, \mu bar$. A time step of 60 s is used in the calculations. With the resolutions described above, a 1-day simulation requires 12 hours of computation on a Silicon Graphics Origin 2000 System at 300 MHz clock speed. All simulations required 12 Titan days to reach energy balance in which globally integrated sources equal the sinks, while steady state dynamics were achieved sooner, after around 8 Titan days.

The coupled non-linear differential equations listed in section 2.2 are solved in the code by explicit time-step integration at each grid point. First and second order derivatives are calculated as finite differentials using the expressions

$$\frac{\partial f}{\partial a} \approx \frac{f_{j+1} - f_{j-1}}{2\Delta}, \tag{12}$$

$$\frac{\partial^2 f}{\partial a^2} \approx \frac{f_{j+1} - 2f_j + f_{j-1}}{\Delta^2}, \tag{13}$$

where $\Delta = a_j - a_{j-1} = a_{j+1} - a_j$ is the grid spacing used for variable a. Changes of momentum and energy are calculated at each time step using (4), (5), and (8) and added to the current parameter values. A numerical smoothing algorithm is used at around every tenth time step to account for buildup of numerical errors. The calculation of vertical winds w is not performed using the third dimension of equation (1), but by solving the equation of continuity (7). Values of w are calculated by stepping from the model's upper boundary down to the layer of interest n using a fourth-degree Taylor expansion

$$\begin{aligned} w^n &= w^{n+1} - \frac{\partial w}{\partial n} - \frac{1}{2}\frac{\partial^2 w}{\partial n^2}\Delta n^2 \\ &- \frac{1}{6}\frac{\partial^3 w}{\partial n^3}\Delta n^3 - \frac{1}{24}\frac{\partial^4 w}{\partial n^4}\Delta n^4. \end{aligned} \tag{14}$$

For numerical reasons we assume $w = 0$ at the upper boundary, and the partial derivatives of w with n used in (14) are expressed through the horizontal wind divergence, using (7) and the relation

$$\frac{\partial}{\partial n} = \frac{\partial p}{\partial n}\frac{\partial}{\partial p} = -\alpha\, p\, \frac{\partial}{\partial p}, \tag{15}$$

where α is the vertical resolution in fractions of a scale height, as previously introduced in (11). We obtain the total vertical velocity in the height frame v_z by adding the wind relative to a pressure level $-1/(\rho g)w$, and the velocity of the pressure level itself: $v_z = (\partial h_p/\partial t) - 1/(\rho g)\, w$, where h_p denotes the altitude of the pressure level. Note that we do not assume $v_z = 0$ at the top boundary, still allowing for the expansion and contraction of the atmosphere there. Although v_z is not used in the actual calculations, it is computed as output parameter.

We have followed the usual approach of employing log pressure rather than altitude as the vertical coordinate. This change of variables is only strictly correct in a plane-parallel atmosphere with constant gravity. With the acceleration of gravity and the size of a differential volume element decreasing by around 40% over the extent of Titan's thermosphere, this approximation must be used with caution. A more accurate approach would be to retain geometric altitude as the vertical coordinate. However, this changes the form of the continuity, momentum, and energy equations and to implement it requires creating a new GCM code. Rather than undertake this massive enterprise at this time we attempt to estimate the potential errors due to the log pressure approach. In essence, the continuity equation (7) contains the intrinsic assumption of constant g and will have an additional term when employing a rigorous treatment with non-constant g. Numerical experiments have shown this additional term to be around 4% of the horizontal divergence term in (7). In addition, we carried out simulations in which we set the gravity on Titan to a height-independent mean value, which is unrealistic for the planet, but mathematically more consistent when using pressure coordinates. These experiments revealed that the dynamics were similar to those presented in this paper. So the use of pressure coordinates combined with height-dependent gravity appears to have little effect on the overall results.

3. Comparison of Globally Averaged 3-D Model With 1-D Model

3.1. Potential Differences Between 1-D and Averaged 3-D Calculations

One-dimensional thermal models have a long and illustrious history in planetary science and are very useful, if employed properly. They have the distinct advantage that, because of computational time constraints, more physics can be included than in 3-D

models. Our investigation has already benefited from this because we rely on the 1-D models of *Yelle* [1991] to choose the altitude regions, constituents, and radiative heating sources in the 3-D models. Three-dimensional models can also be used to investigate the consequences of the global-averaging inherent in 1-D models. It is therefore of interest to compare 1-D models with the global average of 3-D models. There are four potential sources of differences between the 1-D model and the global mean: (1) Changes in the vertical structure of the atmosphere with latitude or local time can alter the solar heating rate profile, producing a different value than for an assumed, globally uniform atmosphere. (2) The global average of the radiative cooling rate may differ from the radiative cooling rate calculated at a globally averaged temperature. (3) The global average of the thermal conduction rate may differ from the thermal conduction rate for a globally averaged temperature profile. (4) Dynamical terms may not average to zero. The first effect occurs only in an extended atmosphere where variations in gravity and differential volume elements are large enough to be important. In addition, horizontal temperature variations must be large enough to significantly alter the altitude of pressure levels. The Titan thermosphere covers about 12 scale heights, implying that horizontal temperature variations of order 10% or larger could cause significant changes in the solar heating rate at a given pressure level. The second and third effects are related to the fact that radiative cooling and thermal conduction depend non linearly on temperature. If the temperature perturbations are large enough for linear expansion about the global mean to be a poor approximation to these rates, then the 1-D calculations and global-average calculations could differ significantly.

The 1-D model calculations presented here differ from those by *Yelle* [1991] primarily in the way that globally averaged solar heating rates are calculated. In the calculations presented below we compute the heating rate on a latitude and local time grid and average the individual height profiles to obtain a mean. The same atmosphere is used for each point on the grid, but the changes in solar illumination geometry are accounted for. Spherical geometry is used with a numerical integration to determine the column abundance along the line of sight to the Sun, rather than the plane parallel assumption. Precisely the same algorithm is used in the 3-D GCM, with the only difference that the 3-D code considers the global differences in temperature, which have a small effect on the scale heights of constituents and pressure level altitudes. Results from the 3-D calculations revealed that the altitude of the top model boundary (near 1400 km height) at equinox and solar maximum is around 5 km lower at the poles than at the equator, which is around 5% of a scale height there (95 km) and thus minor only. The calculations by *Yelle* [1991] differed in that they estimated globally average heating rates by calculating the heating rate at a solar zenith angle of 60° and applying a factor of 0.5 for diurnal averaging. For consistency with the 3-D code we have also altered the heating efficiencies in the 1-D code to values of 0.5.

3.2. Comparison of Heating Rates

Figure 3 shows vertical profiles of globally averaged rates of solar heating (solid lines), radiative cooling through HCN (narrow-dashed), and cooling by vertical molecular conduction (dotted), as computed by the 3-D GCM (triangles) and the 1-D model (asterisk) for solar minimum and maximum conditions. Furthermore, it shows the rates of heating by horizontal advection (wide-dashed) and cooling by vertical advection (dashed-triple dotted), as computed with the 3-D GCM only, since these terms involve the dynamics which are not calculated in the 1-D model. The solar heating curves in Figure 3 peak near the 10 and 0.1 nbar pressure levels, corresponding to around 750 and 1000 km altitude. The lower of these peaks is to 75% caused by absorption of the Lyman α line (1216 $\mathring{A}$) through CH_4, with the remaining 25% of the heating coming from other wavelengths above 800 $\mathring{A}$. The upper of these peaks is for solar minimum (maximum) conditions to 27% (18%) caused by absorption in the Lyman α line and to 16% (12%) by the He II line (304 $\mathring{A}$) absorption. The He II absorption is mainly due to N_2 (90%) and partly due to CH_4 (10%). The remainder of heating at 0.1 nbar is due to other wavelengths both above (45%) and below (55%) 800 $\mathring{A}$. Note that vertical conduction (dotted) acts as an important energy source between heights of the solar heating peaks by vertically distributing the solar energy. Figure 3 also shows that conduction is the main energy sink above the 10 pbar (1 pbar) pressure level at solar minimum (maximum), or around 1200 (1450) km altitude, being more important than the HCN radiative cooling which dominates at the lower altitudes.

The curves from both models generally show a good agreement, with some discrepancies occurring mainly above 0.1 nbar (1000 km), where the 1-D heating rates are around 20% larger than those from the 3-

D model. Similarly, the HCN cooling rates are larger in the 1-D code by roughly the same amount above 1000 km and differ at lower altitudes by less than 2%. The differences below 1000 km are generally smaller at solar maximum, except for altitudes below 700 km where they reach 12%. So discrepancies in the HCN cooling are found primarily where the heating differs as well, suggesting that they react to the differences in heating. The conductive cooling (dotted) is slightly larger in the 3-D code. There is some heating in the 3-D GCM by horizontal advection (wide-dashed) peaking near the 0.05 nbar (1100 km) level with rates of around 5 (8)% the solar heating rate at that height for solar minimum (maximum). Furthermore, the figure shows cooling by vertical advection (dashed-triple dotted) peaking near the 0.1 nbar (1000 km) level at around 4 (6)% the HCN cooling rate for solar minimum (maximum) conditions. At other altitudes the effects of advection were found to be significantly smaller. Note that the solar heating algorithm used in the 1-D code is identical to that used in the 3-D code after globally averaging (see section 3.1), so when using heating schemes which assume a fixed solar zenith angle, such as those by *Yelle* [1991] the discrepancies between 1-D and 3-D simulations may be larger than those found here. Furthermore, the 3-D code currently uses constituent mixing ratios which are globally constant on a fixed pressure level. When allowing for variations in composition with latitude and longitude, the solar heating curves from the 3-D code in Figure 3 might be affected. Finally, dynamical effects such as upward propagating gravity waves and their deposition of heat are not considered in the 3-D calculations at present and may have an important influence on the thermal structure, giving rise to further differences between the 1-D and 3-D calculations. Their effects will be the subject of future studies with the GCM.

Of the potential reasons for discrepancies between the 1-D and 3-D codes listed in section 3.1 the most significant one appears to be item 1, the fact that 3-D calculations consider latitudinal and local time changes in the vertical structure of the atmosphere. These cause differences in heating which then generate discrepancies in the radiative HCN cooling and vertical conduction. On the other hand, averaging globally the radiative cooling rates calculated from 3-D temperature profiles seems to produce values very similar to the rates calculated from globally averaged temperatures (item 2 of list in section 3.1). Whether the same applies to the thermal conduction rates (item 3) is difficult to establish from our simulations since significant part of the discrepancies of dotted curves in Figure 3 is caused by differences of the solar heating profiles in 1-D and 3-D simulations. The dynamical terms (item 4 in 3.1) are found to account for around 5-10% of the heating at some heights above 0.1 nbar, while below that winds in these simulations (see section 4.3) are too small. Even though heating and cooling through horizontal and vertical advection are of the same magnitude, they do not average out to zero at any given altitude since their peaks appear at different altitudes.

Table 1 shows the heating and cooling rates calculated in the GCM and integrated over latitude, longitude, and the vertical extent of the thermosphere. These calculations show that the primary balance is between solar heating and radiative cooling by HCN. Other terms are roughly 2 orders of magnitude less important; thus, solar heating and HCN cooling account for virtually all the energy flow into or out of the system. In fact, the vertical and horizontal advection terms nearly cancel, making the balance between solar heating and HCN cooling even more accurate. Although the vertical conduction, horizontal advection, viscous heating and vertical advection terms are negligible on a global scale, they can be important locally. One example of this is shown in Figure 3, where thermal conduction is important in some altitude ranges. Also, we show in section 4.1 that these terms can be important at specific latitudes and local times, thereby affecting the temperature and wind distributions, if not the overall energetics of the thermosphere.

3.3. Comparison of Temperatures

Vertical profiles of temperatures in Titan's thermosphere are shown in Figure 4 for solar minimum and maximum conditions. The globally averaged temperatures from the 1-D simulations are around 1-2.5 K (0.3-1.0 K) higher than those from the 3-D simulations at solar minimum (maximum), corresponding to less than 1.6% discrepancy. So the 3-D globally averaged temperature profile is virtually identical to that from the 1-D simulations but shifted toward slightly lower values, particularly at solar minimum. The discrepancy is consistent with that found in the solar heating rates at higher altitudes and cooling rates at lower altitudes (see discussions in 3.2). Although at higher altitudes the cooling rate is also larger in the 1-D simulations, it does not fully compensate for the stronger solar heating. Overall, the differences in

heating rates between the 1-D and 3-D simulations translate into negligible globally averaged temperature differences. So for Titan the use of 1-D models appears to be an acceptable approximation for calculations of solar-driven energetics.

Figure 4 shows that the day-night temperature difference at the top of the thermosphere on Titan is of around 8 (18) K at solar minimum (maximum), or 5 (10)% the average temperature. On Earth thermospheric day-night temperature differences reach 200 K, or 25% at solar minimum, on Mars they reach 40% and on Venus 80% [*Bougher et al.,* 1999], so the variations on Titan are very small in comparison. The figure also shows that Titan's thermosphere below 1000 km has virtually no day-night temperature variation. The globally averaged temperature curve in Figure 4 is closer to the dayside than to the nightside values because of nightside heating at high latitudes, as discussed further in section 4.1.

4. Thermospheric in Situ Dynamics and Energetics

4.1. Heating Terms

Figure 5 shows the energy equation terms for equinox solar maximum conditions at latitude 60° N and four different pressure levels versus longitude. The subsolar point is located at 0° longitude ("noon"), while the antisolar point is at 180° ("midnight"). The figure illustrates a number of important features which are described in the following.

The solar heating term (solid) is, as expected, largest at day and smallest at night. However, the plot shows that above 1000 km (0.1 nbar) the nighttime solar heating does not decrease entirely to zero values. This behavior was in section 2.4 explained from the geometry of Titan's atmosphere. Solar heating expands well into the high-latitude nightside thermosphere poleward of around 60°N at sufficiently high altitudes since the planet's shadow is too small to cover the entire thermosphere at night. For lower heights the thermosphere is optically thicker, so the radiation does not reach as far into the nightside as for higher altitudes. The effect of nighttime heating found in Figure 5, which is for 60°N, becomes considerably stronger at higher latitudes. At 72°N (not shown) the nighttime heating is of around 50% the daytime heating rate. This has important implications on the thermally driven wind system, as discussed in section 4.2.

Figure 5 shows that Titan's nightside is heated also at lower latitudes by two other processes, horizontal advection (wide-dashed) and, particularly below the 10 pbar (1200 km) level, adiabatic heating (dashed-dotted). Vertical advection (dashed-triple dotted) is also found to play a role on the nightside but less than the other two. Principal daytime cooling processes shown in Figure 5 are HCN radiative cooling (narrow-dashed) below 1200 km and vertical conduction (dotted) above that. While the former remains roughly constant throughout the day, the latter is strongest at day and lower at night. Below 1200 km the dayside temperature is reduced also by adiabatic cooling. So adiabatic processes appear to equalize the day-night temperature gradient on Titan by cooling at day and heating at night. This explains the relatively small day-night temperature variations, particularly below 1000 km.

4.2. Acceleration Terms

Meridional and zonal acceleration terms are plotted in Figures 6 and 7, respectively, for the same locations and conditions as the energy terms of Figure 5. Horizontal pressure gradients are in the model given in the form of gradients of the geopotential height of a pressure level. Following the hydrostatic equation, the two are linked through the simple relationship $\partial p/\partial x = -1/(\rho g)\partial h_p/\partial x$. The terms labelled "Geopot" in Figures 6 and 7 are the geopotential height gradients. In the following discussions we nevertheless refer to them using the more familiar term "pressure gradient" since the two quantities are roughly proportional on a pressure level. The terms of horizontal viscosity are not shown in Figures 6 and 7 since they are negligible at all times, compared with all the other acceleration terms.

From Figures 6 and 7 it is evident that dynamics above 1000 km are essentially controlled by the balance between pressure gradients (solid) and vertical viscosity (wide-dashed). Although at mid-latitudes to high-latitudes other terms also become large, particularly the Coriolis force (dashed- dotted), horizontal advection (dashed-triple-dotted), and curvature acceleration (dotted), the latter two balance each other, thus not contributing to the overall behavior determined by the pressure- viscosity balance. At high latitudes only the Coriolis force plays an observable role, giving an eastward (westward) acceleration during daytime (nighttime) when winds blow poleward (equatorward) and giving an equatorward (poleward) acceleration at dusk (dawn) when the zonal winds

blow eastward (westward). It is important to realize also that the geostrophic approximation, often used on Earth, does not apply in Titan's thermosphere according to these simulations since pressure gradients are not balanced by the Coriolis forces. With pressure gradients being balanced by viscosity, the winds overall flow perpendicular to the isobars rather than parallel, which is also discussed in section 4.3. Transport of momentum through vertical advection (narrow-dashed) plays a minor role only. It does become stronger relative to the other terms at 1000 km and below, but there the overall accelerations are too small to drive significant winds.

As outlined in section 1, *Rishbeth et al.* [2000] predicted that curvature forces would play a key role in the dynamics on Titan and be balanced in the meridional direction by the equator-to-pole pressure gradient, resulting in an essentially zonal flow. From Figure 6 we see that meridional curvature forces do become large, particularly in the dawn and dusk sectors (90° and 270° longitude) where zonal winds are particularly strong (see discussions in 4.3 and the curvature term in (4), but they are balanced by the horizontal advection terms, not by the pressure gradient. The same applies to the zonal components. Below around 1000 km all accelerations in the solar-driven thermosphere are two orders of magnitude smaller than those at 1200 km since the day-night temperature and pressure gradients have virtually disappeared (see the dashed and dotted lines in Figure 4 and the solid lines in Figures 6 and 7). As a result, the discussed balances which are found at higher altitudes do not always apply at lower heights as well, but with no implication on the winds which are close to zero when driven by solar heating alone.

When longitudinally (diurnally) averaging the meridional acceleration terms and plotting them versus latitude (not shown), we find that the balance between curvature and horizontal advection as well as pressure and viscosity persists at all latitudes. The longitudinally averaged accelerations in the zonal direction are about an order of magnitude smaller than the meridional ones, so averaged over a Titan day there is stronger acceleration in the meridional than in the zonal direction. At solstice (not shown) the basic behavior and balance of acceleration terms is similar, but some differences occur due to the interhemispheric flow from summer to winter, leading to stronger effects of Coriolis force and advection.

4.3. Global Temperatures and Winds

In the following we present the global temperature and wind profile calculated by the 3-D Titan GCM at equinox and Southern Hemisphere solstice. Globally averaged temperature profiles from these simulations are shown in Figure 4. The equinox simulation was carried out for solar maximum conditions, while the solstice simulation is for solar minimum, similar to the conditions expected during the anticipated commencement of Cassini measurements in late 2004. The two simulations were carried out by starting from two different globally averaged altitude profiles of temperature and composition. We make no attempt to evaluate the transition between equinox and solstice and therefore did not start one simulation from the other. Both simulations were run to steady state, which required 12 Titan days. It is remarkable how quickly the thermosphere reaches steady state conditions, while calculations for Titan's stratosphere by *Hourdin et al.*[1995] required several Titan years, which is due to the much longer radiative transfer time scales at lower altitudes on Titan. Simulations by *Bougher et al.*[1999] also found the thermospheres of Venus and Mars to reach steady state rapidly as a result of strong IR cooling.

Figures 8 and 9 show global profiles of temperatures and superimposed horizontal winds at equinox and solstice, respectively, on the 0.1 nbar (around 1000 km) and 1 pbar (around 1300 km) pressure levels. The plots are snapshots at a fixed universal time, but the longitude axis may be regarded equivalent to a local time axis with noon and midnight located at longitudes 0° and 180°. The figures confirm earlier findings that the day-night temperature difference near 1300 km is of around 10 (20) K at solar minimum (maximum), with peak winds of 30 (60) m/s. These values reduce to 1.5 (3) K and 5 (8) m/s near 1000 km altitude. We carried out additional simulations for equinox at solar minimum as well as solstice at solar maximum (not shown) and found the day-night temperature differences as well as peak wind values at any given level of solar activity to be independent of season, thus depending only on the level of solar activity.

In the following we will discuss features near 1300 km altitude (top panels in Figures 8 and 9) which represent exospheric conditions on Titan. Both figures show that winds blow essentially from day to night perpendicular to the isotherms (and isobars), which is a consequence of the balance between pressure gradients and viscosity (see discussions in section 4.2).

Unlike Earth with its auroral oval, they blow undisturbed over the polar regions on Titan. The dayside and nightside temperature extrema are located near 15° and 195° longitude, respectively, corresponding to a shift toward later local times with respect to the subsolar and antisolar points by 1/24 of a Titan day. As pointed out in section 4.1, horizontal advection plays an important role in the energy balance, and results from Figures 8 and 9 indicate that it has an observable effect on the temperature profile, shifting the daytime and nighttime extrema toward later local times. Note that winds as small as 10 m/s are sufficient to cause advection over 28° latitude or longitude on Titan within 1/8 Titan day, due to its slow rotation rate. The phases of temperature are latitude dependent both at solstice and equinox; the maximum (minimum) occurs at the subsolar (antisolar) point near the poles and is shifted toward later local times closer to the equator. This behavior is a result of the global wind pattern properties.

The rotational velocity on Titan at 1300 km altitude has a value of around 18 m/s at the equator and 9 m/s at 60° latitude, implying that solar-driven zonal winds reach superrotating velocity values during most of the day, except at noon and midnight when they become smaller. This is in contrast to the situation usually encountered on Earth, where rotational velocities are in the order of 400-500 m/s in the thermosphere and typical zonal winds are below that, except near the auroral oval. So solar forcing alone is enough on Titan to create superrotating velocity values, mainly because of the small rotation period. Note, however, that there is no net solar-driven superrotation on Titan since zonal averages of winds in Figures 8 and 9 reach values of below 3 m/s which are smaller than the rotational velocity values.

While temperatures at equinox on the dayside are relatively uniform with latitude, decreasing by around 5 K from equator to pole (see Figure 8), the feature of nighttime solar heating at high- latitudes (see section 4.1) causes a sharper temperature gradient on the nightside by around 14 K from pole to equator. As result of the temperature gradient behavior, nighttime equatorward winds are stronger than the daytime poleward winds. For 60° latitude meridional wind values are around 35 m/s at day and 45 m/s at night. At solstice (Figure 9) the entire high-latitude winter hemisphere is not illuminated at night, while on the summer hemisphere the region of nighttime heating reaches more equatorward by around 15° than at equinox. Therefore, nighttime latitudinal temperature gradients are sharper on the summer hemisphere than on the winter hemisphere, while the dayside latitudinal gradients are sharper in the winter hemisphere. This behavior is also reflected in the meridional winds. On the winter hemisphere the dayside poleward winds are stronger than nightside equatorward winds, while on the summer hemisphere the opposite is found. At 60° latitude typical daytime meridional wind values in the summer (winter) hemisphere are 10 m/s (25 m/s), while nighttime values are 25 m/s (15 m/s). So the high-latitude nighttime solar heating leads to interesting features in the meridional winds.

Near 1000 km (bottom panels in Figures 8 and 9) the day-night temperature gradients are below 3 K, so the winds are considerably weaker, too, with values below 8 (5) m/s at solar maximum (minimum). Nevertheless, the global patterns show some interesting features we will point out here. It was discussed in section 4.2 (see also Figures 6 and 7) that Coriolis force plays an increasingly important role when moving down in altitude in Titan's thermosphere. One important feature in Figures 8 and 9 are the cells of anticlockwise (clockwise) circulation in the Northern (Southern) Hemisphere in the dawn sector (near 240° longitude), a manifestation of Coriolis acceleration. Inevitably, the profile at solstice is asymmetric around the equator. A further consequence of Coriolis forces is the fact that the eastward components of mid-latitude and high-latitude winds in the dusk sector (near 90° longitude) are generally larger than westward components of those in the dawn sector. Other than at 1300 km, the wind vectors at 1000 km are often not perpendicular to the isobars (isotherms), indicating that pressure gradients are not only balanced by vertical viscosity, as is the case for the higher altitudes. Also, there is virtually no nighttime heating at 1000 km altitude (see Figure 5) as a result of changes in geometry and the larger optical depth, so the nighttime temperatures are fairly uniform with latitude. This applies to equinox conditions as well as solstice. As a result, meridional pressure accelerations are very small at night, as shown also in Figure 6 (solid curve in panel for $n = 15$). Overall, therefore Titan's thermosphere near 1000 km resembles more the terrestrial one when ignoring effects of the ionosphere.

4.4. Comparisons Between Titan, Earth, Mars, and Venus

The basic behavior of solar-driven thermospheric dynamics on Titan may be compared to that on Earth, Mars, and Venus. Mars is the smallest of these three terrestrial planets with a radius of 3440 km, which is only 33% larger than Titan's. However, in terms of planetary rotation speed, Titan (15.8 days) resembles Venus (117 days) in that both are slow rotators. When considering the basic equations of dynamics and energetics, a smaller planetary radius enhances the importance of spherical terms such as curvature, divergence and advection (see (2) and (3)), while slow rotation speeds reduce Coriolis forces and also favor advection. The fundamental parameters of planetary radius and rotation speed explain some of the features in the thermospheres of Earth, Mars and Venus which were described in detail by *Bougher et al.* [1999]. On Venus, temperatures are determined largely by solar heating, CO_2 IR cooling and, on the nightside, adiabatic heating and horizontal advection. On Mars and Earth the energy balance is determined largely by solar heating, adiabatic heating and cooling and vertical conduction. In the terrestrial case additional energy input is provided at mid to high latitudes by joule heating and magnetospheric particle precipitation. Titan has in common with Venus the importance of adiabatic nightside heating and advection, but with Mars and Earth the importance of vertical heat conduction and adiabatic daytime cooling. Adiabatic processes are particularly important on Mars, due to its small planetary radius, which leads to strong vertical winds from horizontal wind divergences. Pressure gradients are on Venus balanced by viscosity and wave drag, while on Mars the spherical terms become important as well and on Earth ion-neutral drag plays a key role. A further similarity between Titan and Venus lies in the fact that in situ thermospheric and stratospheric superrotating winds are found on both planets. *Bougher et al.* [1999] showed this superrotation on Venus to cause asymmetries in the dawn and dusk winds. In spite of some similarities between Titan and these three terrestrial planets, therefore, the dynamics on Titan are in many ways very different and unique.

5. Role of Vertical Dynamical Coupling

5.1. Introduction: Stratospheric Jets on Titan

The calculations presented in section 4 show the response of Titan's atmosphere to solar heating only, ignoring any contribution from above (through magnetospheric forcing from Saturn, see also section 1) or below (from stratospheric and mesospheric winds). It is well known that the Earth's thermosphere is considerably influenced by dynamical and energetic coupling across the mesopause, so in the following we will investigate how stratospheric and mesospheric winds on Titan might influence the thermospheric wind profiles.

Titan's atmospheric temperature, pressure, haze optical depth and zonal winds for the height range of 250 to 450 km were derived by *Hubbard et al.* [1993] from the occultation of 28 Sgr in July 1989. The authors found the presence of strong zonal jets in that height regime with peak velocities of 175 m/s at high midlatitudes (74°). At the time of occultation the Northern Hemisphere was more opaque than the Southern Hemisphere because of thick haze, so their measurements were more reliable for the Southern Hemisphere. Hubbard et al. initially measured the latitudinal pressure profile and derived that pressure values were larger at the equator, a deformation which they attributed to the zonal winds. Winds were then calculated from the pressure profile under the assumption of gradient wind balance, given by

$$2\Omega u_\varphi cos(\theta) + \frac{u_\varphi^2}{a \cdot tan(\theta)} = -\frac{1}{\rho a}\frac{\partial p}{\partial \theta}. \qquad (16)$$

Here the meridional pressure gradient (right side) is balanced by the meridional components of Coriolis acceleration (first term on left side) and centrifugal acceleration (second term on left side). The zonal wind is given by u_φ, θ is the colatitude and other variable symbols in (16) are defined as for (4) and (5). Because of Titan's slow rotation period the centrifugal term of (16) dominates over the Coriolis term. Combining (16) with the hydrostatic equation and the ideal gas law yields the thermal wind equation which expresses latitudinal gradients of temperature as a function of vertical gradients of zonal winds. The rotational velocity at 450 km altitude on Titan lies between 14 m/s at the equator and a few m/s at high latitudes, so the zonal winds found by Hubbard et al.

are strongly superrotating. Superrotation in Titan's stratosphere was also suggested by *Flasar et al.* [1981] on the basis of Voyager 1 data. It is believed that this superrotation, like that on Venus, is prograde (in the sense of the planetary rotation), although measurements give no conclusive evidence of the wind direction. Meridional winds are assumed to be very small and thus negligible.

The presence of zonal jets in Titan's stratosphere was also reproduced by numerical simulations with three-dimensional general circulation models of Titan's stratosphere by *Hourdin et al.* [1995] and *Tokano et al.* [1999]. While simulations by Hourdin et al. intrinsically generated superrotating winds in Titan's stratosphere, those by Tokano et al. reproduced super-rotation only after applying artificial damping to the meridional stratospheric circulation. The numerical simulations by Hourdin et al. support the idea first proposed by *Gierasch* [1975] for Venus, that superrotation is generated by upward transport of angular momentum as a result of the meridional circulation. *Zhang et al.* [1996] found through numerical modeling that dawn-dusk asymmetries in the drag associated with dissipating gravity waves could account for super-rotation in the Venusian thermosphere. It is beyond the scope of this study to investigate in further depth the causes of super-rotation on Titan.

Note that the observations of 28 Sgr took place during Northern Hemisphere solstice on Titan (see Figure 1), while the zonal wind profiles derived by *Hubbard et al.* [1993] are symmetric around the equator, a situation expected for equinox conditions. As mentioned earlier, the Northern Hemisphere values in these measurements are unreliable, so the symmetry is partly an assumption. Numerical simulations by *Hourdin et al.* [1995] contradicted the symmetry assumption by suggesting stronger zonal winds in the Northern Hemisphere at the time of the occultation of 28 Sgr. However, *Flasar et al.* [1981] derived meridional temperatures profiles for the upper stratosphere from the infrared spectrometer (IRIS) on board Voyager 1 and found the Southern Hemisphere values to be around 3 K warmer than the Northern Hemisphere ones, even though Titan's season at the time of observation was equinox. So there is some ambiguity as to whether the upper stratosphere is in phase with the seasons or not.

In the troposphere the radiative time constant has a magnitude of a Titan year. This indicates that those regions respond only to yearly averaged changes in solar irradiance but not to daily or seasonal ones. The radiative time constant decreases with altitude and in the upper stratosphere (near the 1 mbar level) is only around 20% of Titan's rotation period [*Flasar et al.,* 1981], so the region should be roughly in radiative balance. *Flasar and Conrath* [1990], however, argued that the upper stratosphere follows the slower dynamical timescales rather than the radiative ones. As illustrated by the thermal wind equation, the temperatures and zonal winds are closely coupled, indicating that a seasonal change of the meridional temperature profile must be accompanied by a change in the latitudinal distribution of zonal winds. Any change of zonal wind distribution implies latitudinal transport of angular momentum, which is achieved by meridional winds. Consider an asymmetrical temperature distribution in which the Southern Hemisphere is warmer than the Northern Hemisphere and the Northern Hemisphere latitudinal temperature gradient is sharper than that in the Southern Hemisphere. This roughly corresponds to the situation encountered during the Voyager 1 measurements [*Flasar et al.,* 1981]. At equinox, radiative balance would imply a symmetric temperature and wind distribution around the equator. In our example the Northern Hemisphere temperature gradients are sharper, so zonal winds are stronger there than in the Southern (summer) Hemisphere. Redistribution of momentum is thus achieved by meridional circulation from north to south. This meridional circulation, however, leads to adiabatic cooling and heating by upwelling and downwelling in the Northern and Southern Hemispheres, respectively, so the original asymmetrical temperature profile is partly maintained for as long as the meridional circulation prevails. As a result, both the temperatures and the winds respond to the dynamical timescales which in the stratosphere are comparable to the seasonal timescales [*Flasar and Conrath,* 1990]. So temperature and wind profiles in the stratosphere on Titan may lag behind the solar forcing by around a season. An alternative explanation for the seasonal phase lag was proposed by *Bézard et al.* [1995] who argued that asymmetries in composition and haze alone could account for the observed Voyager temperatures. At present there is too little information available for a definite statement as to whether the stratosphere does have a seasonal phase shift, so for the present purpose we will consider both options.

5.2. Zonal Jets at the Lower Boundary

Both the measurements and simulations give no information about the nature of Titan's circulation between the 1 mbar (450 km) and 0.1 μbar (600 km), introducing a major uncertainty in the lower boundary conditions of our thermosphere GCM. The purpose of discussions here is to provide an estimate of the potential degree of coupling between the lower atmosphere and thermosphere on Titan, so for the present purpose we implemented an elevation profile of the lower boundary pressure level similar to that derived by *Hubbard et al.* [1993], but with reduced values. Essentially, the lower boundary height increases toward the equator symmetrically in both hemispheres, reaching a maximum elevation of 9 km at the equator with respect to the 600 km base altitude. Zonal winds are derived using (16) and have a profile with the same latitudinal shape derived by Hubbard et al., reaching maximum values of around 60 m/s near 60° latitude in both hemispheres, which is around 34% of the peak winds derived by Hubbard et al. The reduction of zonal winds at the higher altitude of our GCM's lower boundary is speculative but partly supported by the simulations of *Hourdin et al.* [1995] which suggest that the stratospheric jets peak near the 1 mbar level and fall off at larger heights. Although those results are partly a consequence of upper boundary conditions in the Hourdin et al. model, they are currently the best available guess. We implemented no longitudinal dependency of lower boundary profiles and meridional winds were set to zero. Note that the zonal jets were implemented only at the bottom boundary level, while above that the atmosphere's response was calculated solving self-consistently the momentum, energy, and continuity equations. To account for the uncertainties regarding the seasonal phase lag of the stratosphere (see section 5.1), the symmetrical forcing was used both in an equinox and solstice simulation. For easier comparison with simulations in section 4.3 we repeated the runs presented there (equinox at solar maximum and solstice at solar minimum), but now with lower boundary forcing. In practice, the forcing had to be implemented gradually with increasing strength, allowing a gentle "spin-up" of the atmosphere. Around 14 Titan days were needed for the lower boundary "spin" to propagate through to the upper levels of the thermosphere.

5.3. Effects of Zonal Jets on Thermospheric Dynamics

Figur

Figure 10 shows latitudinal profiles of zonal winds (positive east) near the 1 pbar (1300 km) level for four different local times (noon, midnight, dusk, and dawn) under equinox conditions at solar maximum. Dashed curves denote the zonal winds from the simulation without lower boundary forcing ("unforced"), while the solid curve is from the simulation with lower boundary jet forcing ("forced"). The unforced simulation results were on a global scale discussed previously in section 4.3. As expected, the overall tendency is for the zonal winds in the forced simulation to be more eastward than in the unforced case. They are stronger eastward by up to 120 m/s over the equator at midnight and dawn and 70 m/s for noon and dusk. Below 1000 km (not shown) the changes become very uniform for all local times, with values of around 100 m/s, due to the absence of significant solar-driven winds, and gradually decrease to the 60 m/s values at the lower boundary. As a result of lower boundary forcing, the previously mainly westward midnight and dawn sector winds are now blowing toward the east. Although we implemented the wind shape derived by *Hubbard et al.* [1993] at our lower boundary, with peaks near 60° latitude, at higher altitudes they transform into wind profiles with peak values at the equator which fall off toward the poles. The reason for this is that the pressure level elevation associated with the Hubbard et al. zonal wind profile is based primarily on the pressure-centrifugal force balance of (16), resulting in peak lower boundary elevation at the equator. In the calculation of the GCM, other terms such as viscosity, advection, and meridional Coriolis forces also play a key role (see section 4.3), so the balance given by (16) is no longer strictly valid above the lower boundary, leading to an adjustment of the latitudinal profile of zonal winds resulting from the implemented pressure level elevation.

Given this shape of the forced zonal wind profile in the middle and upper height range of the model, high-latitude wind values are similar in the forced and unforced cases. When comparing meridional winds from both simulations (not shown), they vary less than the zonal ones, being stronger only by up to 5 m/s at high latitudes. At noon the meridional winds in the forced simulations are stronger poleward and at midnight stronger equatorward. So to a first approximation the lower boundary zonal wind forcing "spins up" the thermosphere and the solar-driven winds appear to a first approximation superimposed almost linearly

onto the rotating atmosphere.

11

Figure 11 shows the global profiles of temperature and superimposed horizontal winds at fixed pressure levels near 1300 and 1000 km altitude from the equinox simulation with lower boundary forcing. This plot can be compared directly to Figure 8, which shows the same simulation but without the lower boundary forcing. Figure 11 shows that the day-night temperature difference is hardly affected by the zonal jets, but the patterns are shifted toward eastern longitudes (later local times) by around 30° (2 /24 of a Titan day) at both altitudes. As a result of the lower boundary forcing the global wind patterns in Figure 11 show not only the generally more eastward drifts at low latitudes to midlatitudes but also two symmetrical circulation cells in the dawn sector near 60° latitude at 1300 km and 85° latitude at 1000 km. The Northern Hemisphere cell consists of anticlockwise and the Southern Hemisphere cell consists of clockwise circulation. The centers of the cells are located where the solar-driven westward (nightward) winds balance those induced by the lower boundary forcing, which are opposite in direction. At lower altitude the solar-driven winds are smaller, while those driven from below are virtually unchanged, so the balance occurs only at higher latitudes, where the lower boundary induced winds become smaller and thus comparable to the solar-induced ones. When applying weaker (stronger) lower boundary winds, the cells thus move equatorward (poleward). The cells are not found in the dusk sector since solar-driven and lower boundary induced winds there point toward the same zonal direction, so no cancellation can occur.

Obviously, the particular patterns in Figure 11 are a result of the lower boundary winds being strongest at the equator. If they were stronger at midlatitudes to high latitudes a single larger cell might appear at low latitudes. The more general message to be read from these simulations is therefore that any winds at 600 km in Titan's atmosphere may have a considerable influence on the global wind pattern in the thermosphere. At present we have too few measurement constraints for a more detailed prediction of thermospheric winds on Titan. These experiments, however, strongly suggest that an experimentally derived global wind profile for the 1000 km regime, as expected from the Ion and Neutral Mass Spectrometer instrument on board Cassini, may provide us with constraints about winds lower down, assuming that they are a superposition of solar and lower atmosphere driven circulation.

Analysis of the acceleration terms reveals that their zonal components are virtually identical in the forced and unforced cases, supporting the idea of a linear superposition. This result is somewhat unexpected, given the importance of the nonlinear terms in the momentum equation (see section 4.2). In the meridional direction, though, the curvature terms become considerably larger equatorward and are balanced by a meridional pressure gradients. So the atmosphere responds to the imposed zonal jets by setting up a meridional pressure gradient to balance the curvature force resulting from the additional winds. This is in accordance with predictions by *Rishbeth et al.* [2000], who found that a zonal flow in Titan's atmosphere is characterized by the balance between meridional pressure gradient and curvature forces. The balance is important particularly below 1000 km, where any solar-driven component is comparatively weak. Our results, in summary, indicate that the solar-driven dynamics are characterized by the balance between pressure gradient and vertical viscosity, while the stratospheric zonal jets in the lower thermosphere cause pressure gradients to be balanced by curvature and Coriolis forces.

At solstice (not shown) the lower boundary forcing essentially has the same influence on dynamics as found for the equinox case. Given that we used a symmetrical wind forcing profile for a solstice case, additional interesting features are found. In particular, the circulation cells found in the dawn sector at equinox now appear at different longitudes (local times) and latitudes. The "winter hemisphere cell" is located more poleward and toward earlier local times, while the "summer hemisphere cell" is more equatorward and toward later local times, compared to the equinox case of Figure 11. Again, this is a consequence of the particular combination of solar and lower boundary driven winds.

Note that the lower boundary forcing we implemented was time independent. For a time-varying wind profile at 600 km the results may be less linear but are beyond the scope of this study. For the case of the Earth's atmosphere, oscillations such as planetary waves, tides, and gravity waves provide the most effective means of vertical coupling between the lower and upper atmosphere. A similar result was shown by *Zhang et al.* [1996] for the case of gravity waves on Venus. These oscillations propagate upward in the atmosphere, with their amplitudes rising as the density decreases, eventually causing dissipation and breaking which deposits large amounts of momentum

and energy into the upper atmosphere. *Rishbeth et al.* [2000] explored the possibility of tidal oscillations on Titan which are generated by the 3% eccentricity of Titan's orbit around Saturn. With Titan's rotation period being identical to its orbital period around Saturn, the same side of Titan always faces Saturn, as for the Earth's Moon. The orbital eccentricity, however, leads to a semidiurnal expansion and contraction of Titan's atmosphere as a result of variations in the gravitational pull of Saturn on Titan's atmosphere. Future 3-D simulations will address this issue in depth.

6. Conclusions

Three-dimensional numerical simulations of the dynamics and energetics of Titan's thermosphere reveal that circulation patterns are forced by variations in solar insolation and coupling to prevailing winds at the lower boundary which may originate from Titan's stratosphere and mesosphere. For the cases investigated here these circulations can be considered independently because they appear to combine in a nearly linear fashion. The solar-driven dynamics on Titan are characterized by the balance between pressure gradients and viscosity, resulting in winds blowing from day to night, approximately perpendicular to the isotherms and isobars. Adiabatic cooling on the dayside and heating on the nightside keeps the atmosphere isothermal to pressures of about 0.1 nbar (1000 km), significantly higher than expected on the basis of radiative time constants alone. The extended nature of Titan's atmosphere implies significantly more solar energy deposition on the nightside of the planet, especially at high latitudes, than on other planets where the ratio of atmospheric scale height to planetary radius is smaller. This effect tends to soften latitudinal variations in temperature. Calculated temperature variations are 4-10%, compared with around 25% on Earth, 40% on Mars, and 80% on Venus. Though the solar forcing is weak on Titan relative to Earth, the lack of ion drag and a weaker viscous force, because of lower temperature, imply the existence of significant winds. We calculate maximum thermospheric solar-driven wind speeds of 30 and 60 m/s at solar minimum and maximum, respectively. The winds forced by circulation at the lower boundary persist to the highest altitudes. This raises the possibility that inference of the winds at high altitudes through measurement of the thermal structure or compositional variations can be used to infer the circulation pattern at lower altitude. Truly realistic models for Titan's upper atmosphere will require more precise information on atmospheric composition, better constraints on energy deposition, better knowledge of conditions in the lower atmosphere, and validation through comparison with observations: results that Cassini is expected to deliver.

Acknowledgments. We appreciate the many helpful suggestions and comments made by the referees. In particular, we acknowledge the considerable efforts of Marina Galand in the checking of our theoretical formulation and for the useful suggestions regarding the logical presentation of results.

This work was supported, in part, by NSF grant AST 9816239 for comparative aeronomy studies. All calculations were carried out on the High Performance Service for Physics, Astronomy, Chemistry and Earth Sciences (HiPer-SPACE) Silicon Graphics Origin 2000 Supercomputer located at University College London and funded by the British Particle Physics and Astronomy Research Council (PPARC).

Janet G. Luhmann thanks Stephen W. Bougher and Marina Galand for their assistance in evaluating this paper.

References

Achilleos, N., S.Miller, J. Tennyson, A.Aylward, I.Müller-Wodarg, and D.Rees, JIM: A time- dependent three-dimensional model of Jupiter's thermosphere and ionosphere, *J. Geophys. Res., 103,* 20,089-20,112, 1998.

Bauer, S.J., *Physics of Planetary Ionospheres*, Springer-Verlag, New York, 1973.

Bézard, B., A. Coustenis, and C.P. Mc Kay, Titan's stratospheric temperature asymmetry: A radiative origin, *Icarus 113*, 267-276, 1995.

Bird, M.K., R. Dutta-Roy, S.W. Asmar, and T.A. Rebold, Detection of Titan's ionosphere from Voyager 1 radio occultation observations, *Icarus 130*, 426-436, 1997.

Bougher, S.W. and R.G. Roble, Comparative terrestrial planet thermospheres, 1, Solar cycle variation of global mean temperatures, *J. Geophys. Res., 96*, 11,045-11,055, 1991.

Bougher, S.W., R.E. Dickinson, R.G. Roble, and E.C. Ridley, Mars thermospheric general circulation model: Calculations for the arrival of Phobos at Mars, *Geophys. Res. Lett., 15*, 1511-1514, 1988.

Bougher, S.W., R.G. Roble, E.C. Ridley, and R.E. Dickinson, The Mars thermosphere, II, General circulation with coupled dynamics and composition, *J. Geophys. Res., 95*, 14,811-14,827, 1990.

Bougher, S.W. , E. C. Ridley, C.G. Fesen, and R. W. Zurek, Mars mesosphere and thermosphere coupling: Semidiurnal tides, *J. Geophys. Res., 98*, 3281-3295, 1993.

Bougher, S.W., J.M. Murphy, and R.M. Haberle, Dust storm impacts on the Mars upper atmosphere, *Adv. Space Res. 19*, 1255-1260, 1997.

Bougher, S.W., S. Engel, R.G. Roble and B. Foster, Comparative terrestrial planet thermospheres, 2, Solar cycle variation of global structure and winds at equinox, *J. Geophys. Res., 104*, 16,591-16,611, 1999.

Burns, A.G., T.L. Killeen, W. Deng, G.R. Carignan, and R.G. Roble, Geomagnetic storm effects in the low-latitude to middle-latitude upper thermosphere, *J. Geophys. Res., 100*, 14,673-14,691, 1995.

Flasar, F.M. and B.J. Conrath, Titan's stratospheric temperatures: A case for dynamical inertia ?, *Icarus 85*, 346-354, 1990.

Flasar, F.M., R.E. Samuelson and B.J. Conrath, Titan's atmosphere: Temperature and dynamics, *Nature 292*, 693-698, 1981.

Friedson, A.J., and Y.L. Yung, The thermosphere of Titan, *J. Geophys. Res., 89*, 85-90, 1984.

Fuller-Rowell, T.J., M.V. Codrescu, R.J.Moffett, and S. Quegan, Response of the thermosphere and ionosphere to geomagnetic storms, *J. Geophys. Res., 99*, 3893-3914, 1994.

Fuller-Rowell, T.J., D.Rees, S.Quegan, R.J.Moffett, M.V. Codrescu, and G.H. Millward, A coupled thermosphere-ionosphere model (CTIM), in *Handbook of Ionospheric Models,* edited by R.W. Schunk, pp. 217-238, Scientific Committee on Solar-Terrestrial Physics, 1996.

Galand, M., J. Lilensten, D. Toublanc, and S. Maurice, The ionosphere of Titan: Ideal diurnal and nocturnal cases, *Icarus, 140,* 92-105, 1999.

Gierasch, P.J., Meridional circulation and the maintenance of the Venus atmospheric rotation, *J. Atmos. Sci., 32,* 1038-1044, 1975.

Hanel, R., et al., Infrared observations of the Saturnian system from Voyager 1, *Science, 212,* 192-200, 1981.

Hourdin, F., O. Talagrand, R. Sadourny, R. Courtin, D. Gautier, and C.P. Mc Kay, Numerical simulation of the general circulation of the atmosphere of Titan, *Icarus, 117,* 358-374, 1995.

Hubbard, W. B., et al., The occultation of 28 Sgr by Titan, *Astron. Astrophys., 269,* 541-563, 1993.

Lellouch, E., Atmospheric models of Titan and Triton, *Ann. Geophys., 8,* 653-660, 1990.

Lellouch, E., A. Costenis, D. Gautier, F. Raulin, N. Dubouloz, and C. Frère, Titan's atmosphere and hypothesized ocean: A reanalysis of Voyager 1 radiooccultation and IRIS 7.7-μm data, *Icarus, 79,* 328-349, 1989.

Letourner, B., and A. Coustenis, Titan's atmospheric structure from Voyager 2 infrared spectra, *Planet. Space Sci., 41,* 595-602, 1993.

Lindal, G.F., G.E. Wood, H.B. Hotz, D.N. Sweetnam, V.R. Eshleman, and G.L. Tyler, The atmosphere of Titan: An analysis of the Voyager 1 radio occultation measurements, *Icarus, 53,* 348-363, 1983.

London, J., G. J. Rottman, T. N. Woods, and F. Wu, Time variations of solar UV irradiance as measured by the SOLSTICE (UARS) instrument, *Geophys. Res. Lett., 20,* 1315-1318, 1993.

National Bureau of Standards, *Properties of Materials at Low Temperature*, Pergamon, Tarrytown, N. Y., 1959.

Rishbeth, H., R.V. Yelle, and M. Mendillo, Dynamics of Titan's thermosphere, *Planet. Space Sci., 48,* 51-58, 2000.

Roble, R.G., E.C. Ridley, A.D. Richmond, and R.E. Dickinson, A coupled thermosphere/ionosphere general circulation model, *Geophys. Res. Lett., 15,* 1325-1328, 1988.

Rothman, L.S., et al., The Hitran molecular database; Editions of 1991 and 1992, *J. Quant. Spectr. Osc. Radiat. Transfer, 48,* 469-507, 1992.

Smith, G.R., D.F. Strobel, A.L.Broadfoot, B.R. Sandel, D.E. Shemansky, and J.B. Holberk, Titan's upper atmosphere: Composition and temperature from the EUV solar occultation results, *J. Geophys. Res., 87,* 1351-1359, 1982.

Strobel, D.F, M.E. Summers, and X. Zhu, Titan's upper atmosphere: Structure and ultraviolet emmissions, *Icarus, 100,* 512-526, 1992.

Tokano, T., F. M. Neubauer, M.Laube and C.P. Mc Kay, Seasonal variations of Titan's atmospheric structure simulated by a general circulation model, *Planet. Space Sci., 47,* 493-520, 1999.

Torr, M.R., and D.G. Torr, Ionization frequencies for Solar Cycle 21; Revised, *J. Geophys. Res., 90,* 6675-6678, 1985.

Yelle, R.V., Non-LTE models of Titan's upper atmosphere, *Astrophys. J. 383,* 380-400, 1991.

Yelle, R.V., E. Lellouch, D. Gautier, and D.F. Strobel, Engineering models for Titan's atmosphere, in *Huygens Science Payload and Mission, Eur. Space Agency Sci. Tech. Rep., ESA SP-1177,* 243-256, 1997.

Yung, Y.L., M.Allen, and J.P. Pinto, Photochemistry of the atmosphere of Titan: Comparison between model and observations, *Astrophys. J. Suppl., 55,* 465-506, 1984.

Zhang, S., S.W. Bougher, and M.J. Alexander, The impact of gravity waves on the Venus thermosphere and O_2 IR nightglow, *J. Geophys. Res., 101,* 23,195-23,205, 1996.

A. D. Aylward and I. C. F. Müller-Wodarg, Atmospheric Physics Laboratory, Department of Physics and Astronomy, University College London, 67-73 Riding House Street, London W1P 7PP, U.K. (alan@apg.ph.ucl ingo@apg.ph.ucl.ac.uk)

R. V. Yelle, Department of Physics and Astronomy, Northern Arizona University, Flagstaff, AZ 86011. (yelle@bohr.phy.nau.edu)

M. Mendillo, Center for Space Physics, Boston University 725 Commonwealth Avenue Boston, MA

02215. (mendillo@bu.edu)

L. A. Young, Southwest Research Institute, 1050 Walnut Street, Boulder, CO 80302. (layoung@boulder.swri.edu)

Received February 17, 2000; revised April 7, 2000; accepted April 18, 2000.

[1]Atmospheric Physics Laboratory, University College London, London, U.K.

[2]Center for Space Physics, Boston University, Boston, Massachusetts

[3]Now at Department of Physics and Astronomy, Northern Arizona University, Flagstaff.

[4]Now at Southwest Research Institute, Boulder, Colorado.

This preprint was prepared with AGU's LaTeX macros v5.01. File titan˙paper formatted May 29, 2002.

Figure 1. Subsolar latitude of Titan between years 1975 and 2010. Also marked are the times of key past and future observations in Titan's atmosphere and the times of solar maximum and minimum. Abbreviations are n.h., Northern Hemisphere; s.h., Southern Hemisphere.

Figure 2. Solar volume heating rates (log_{10} ergs/cm^3/s) for Titan's thermosphere at solar maximum conditions. The plot illustrates the uniqueness of Titan's upper atmosphere geometry which leads to considerable nighttime heating at sufficiently high latitude and altitude. The outer ring represents the thermosphere, while the inner circle is the planet. Dashed latitude grid lines are spaced 15°. Titan's lower atmosphere, between the ring and circle, is assumed to be optically thick.

Figure 3. Globally averaged heating and cooling rates in Titan's upper atmosphere (ergs/cm^3/s), as calculated by the 1-D model of *Yelle* [1991] (asterisk) and the 3-D GCM (triangles) for solar minimum and maximum conditions.

Figure 4. Temperatures in Titan's upper atmosphere, as calculated by the 1-D model of *Yelle* [1991] (asterisk) and 3-D GCM (triangles). Solid lines are the globally averaged values, while the dashed and dotted lines are the dayside maximum ("noon sector") and nightside minimum ("midnight sector") temperature profiles, respectively, which are available only from the 3-D calculations.

Figure 5. Energy terms (ergs/cm^3/s) in Titan's upper atmosphere versus longitude (local time) for different altitudes, as calculated by the 3-D GCM for solar maximum equinox conditions at 60°N latitude. Longitudes 0° and 180° represent the subsolar and antisolar longitudes, respectively.

Figure 6. Same as Figure 5, but for meridional acceleration terms (positive south, m/s^2).

Figure 7. Same as Figure 6, but for zonal acceleration terms (positive east, m/s^2).

Figure 8. Global temperatures and winds on two fixed pressure levels in Titan's upper atmosphere, as computed by the 3-D GCM for equinox conditions at solar maximum. Also indicated are the temperature range, contour level spacing, and maximum wind velocities. Lower boundary winds are set to zero in the simulation.

Figure 9. Same as Figure 8, but for solstice conditions at solar minimum.

Figure 10. Latitudinal profiles of Titan thermospheric zonal winds (positive eastward) near the 1 pbar (1300 km, $n = 23$) level for four different local times (noon, midnight, dusk, and dawn) under equinox conditions at solar maximum. Dashed curves denote the zonal winds from the simulation without lower boundary forcing ("unforced"), while the solid curve is from the simulation with lower boundary jet forcing ("forced").

Figure 11. Same as Figure 8, but for a simulation with zonal jet forcing at the lower boundary.

Table 1. Globally Height-Integrated Heating and Cooling Rates (ergs/s) in Titan's Thermosphere, as Calculated by the Titan GCM for Solar Minimum and Maximum Conditions.

	Solar Heating	Radiative Cooling	Vertical Conduction	Horizontal Advection	Vertical Advection
Solar minimum	1.6×10^{16}	-1.5×10^{16}	1.2×10^{14}	-1.5×10^{14}	1.9×10^{14}
Solar maximum	3.1×10^{16}	-3.0×10^{16}	-1.4×10^{14}	-7.3×10^{14}	8.9×10^{14}

Fig.1

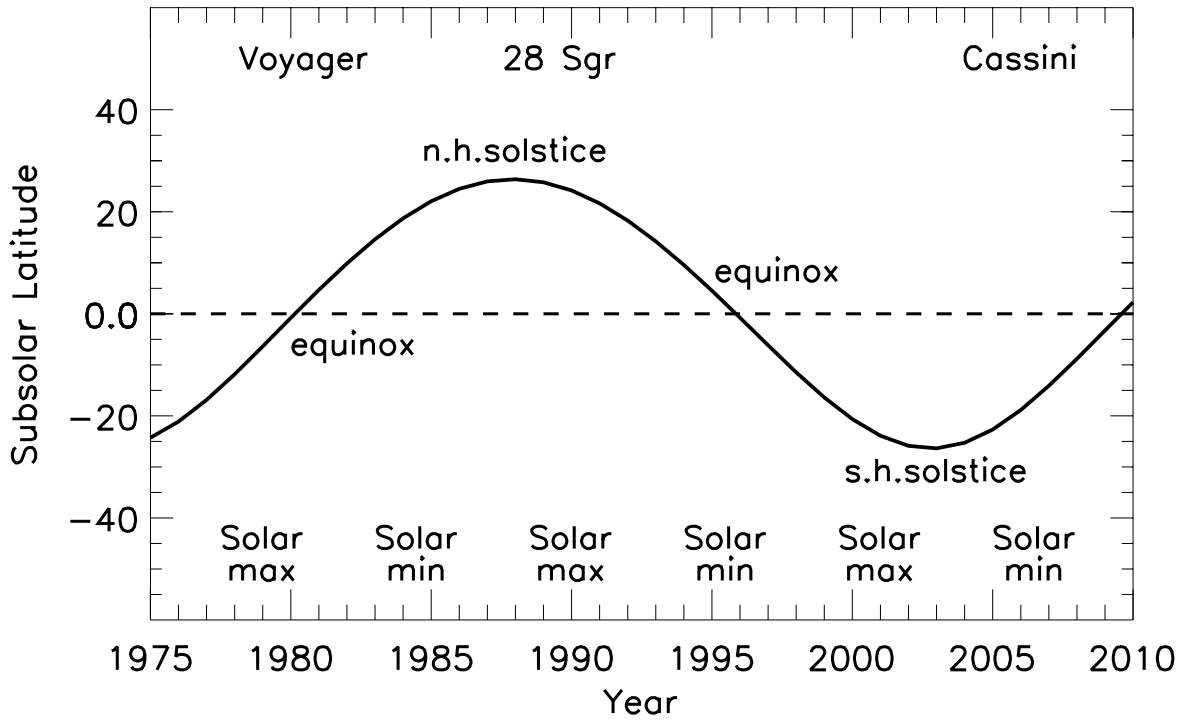
Voyager
28 Sgr
Cassini
40
20
0.0
−20
−40
n.h.solstice
equinox
equinox
s.h.solstice
Solar max
Solar min
Solar max
Solar min
Solar max
Solar min
Subsolar Latitude
1975
1980
1985
1990
1995
2000
2005
2010
Year

Fig.2

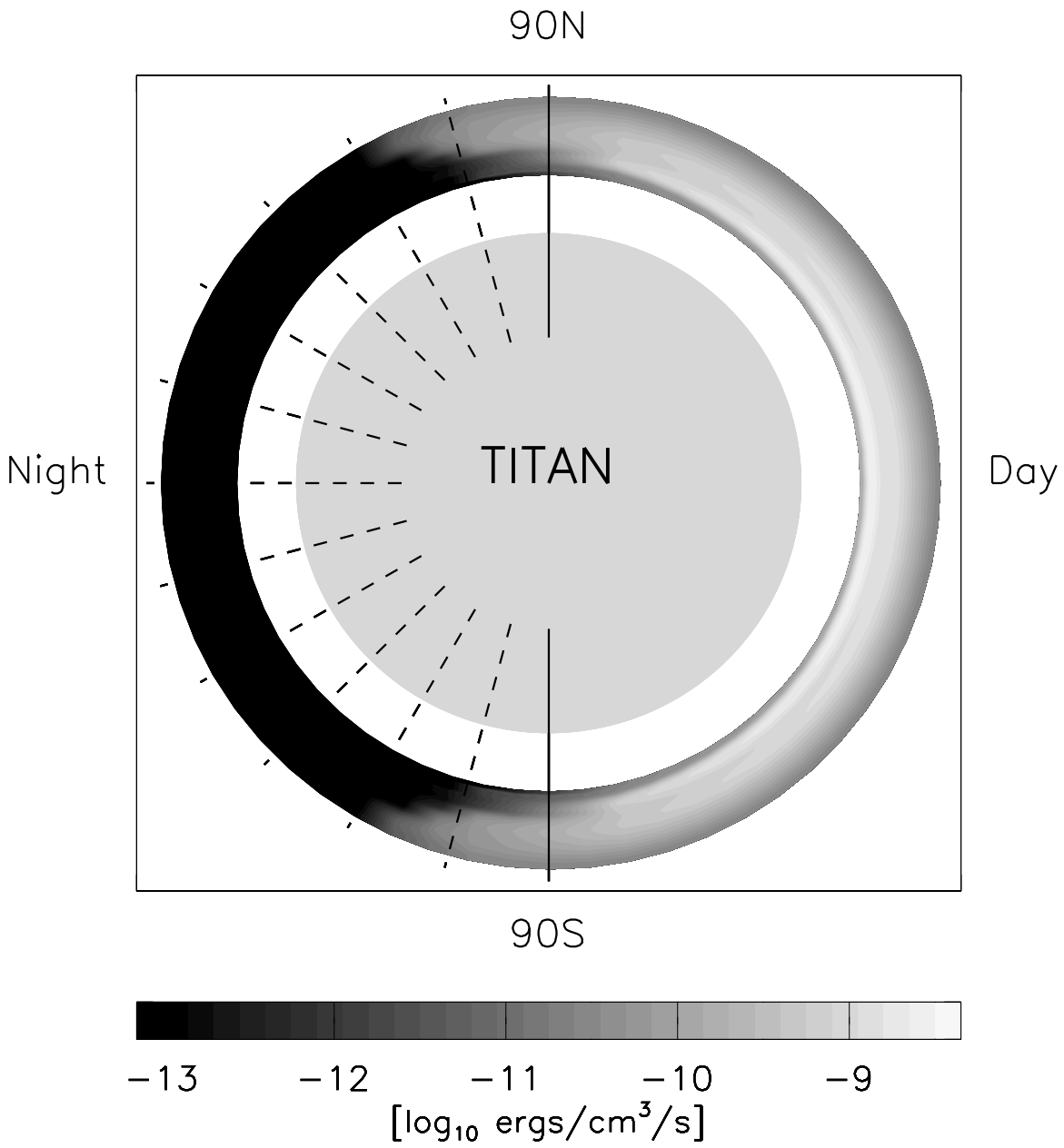

Fig.3

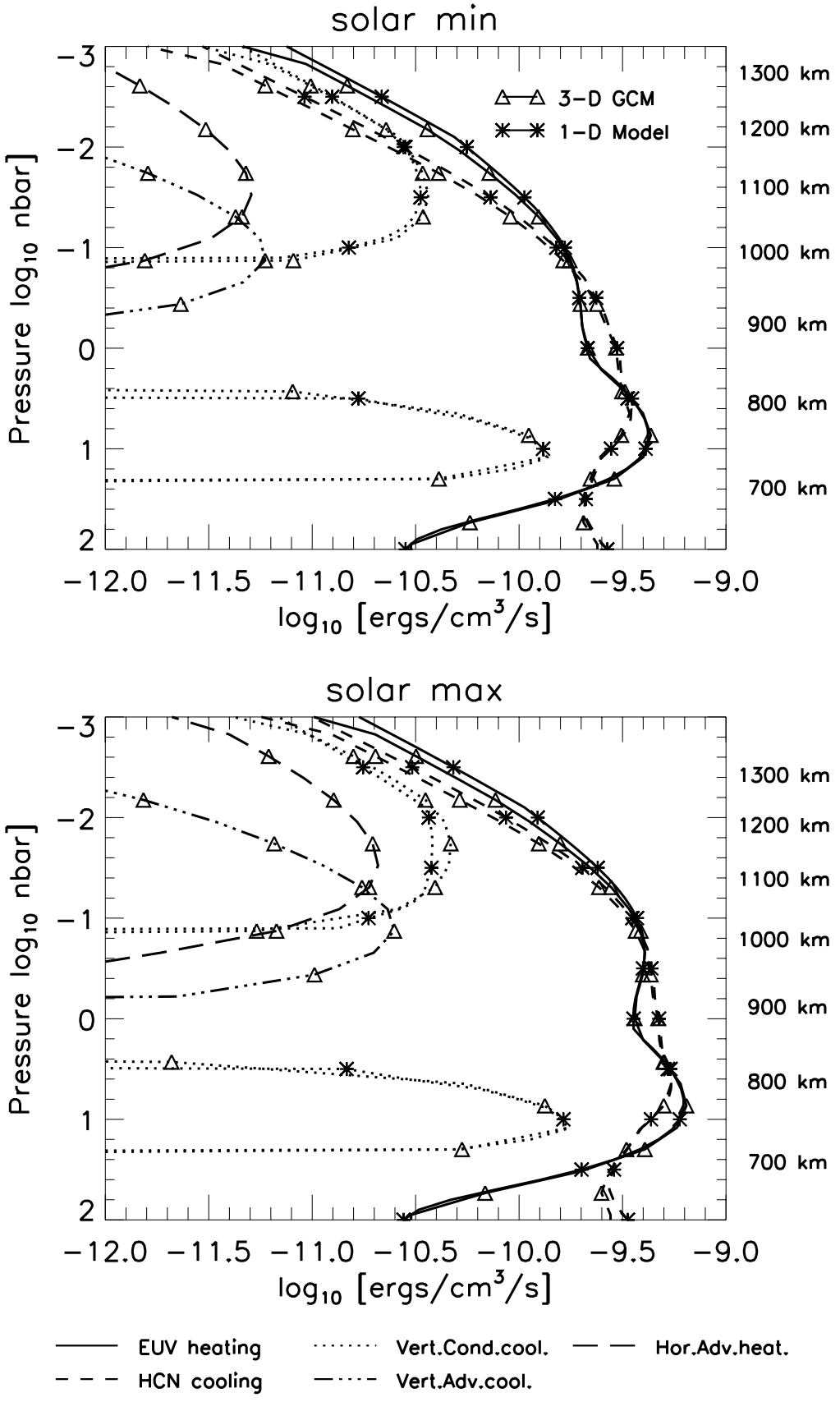
solar min
3-D GCM
1-D Model
Pressure log10 nbar]
−3
−2
−1
0
1
2
1300 km
1200 km
1100 km
1000 km
900 km
800 km
700 km
−12.0 −11.5 −11.0 −10.5 −10.0 −9.5 −9.0
log10 [ergs/cm3/s]
solar max
Pressure log10 nbar]
1300 km
1200 km
1100 km
1000 km
900 km
800 km
700 km
−12.0 −11.5 −11.0 −10.5 −10.0 −9.5 −9.0
log10 [ergs/cm3/s]
EUV heating
HCN cooling
Vert.Cond.cool.
Vert.Adv.cool.
Hor.Adv.heat.

Fig.4

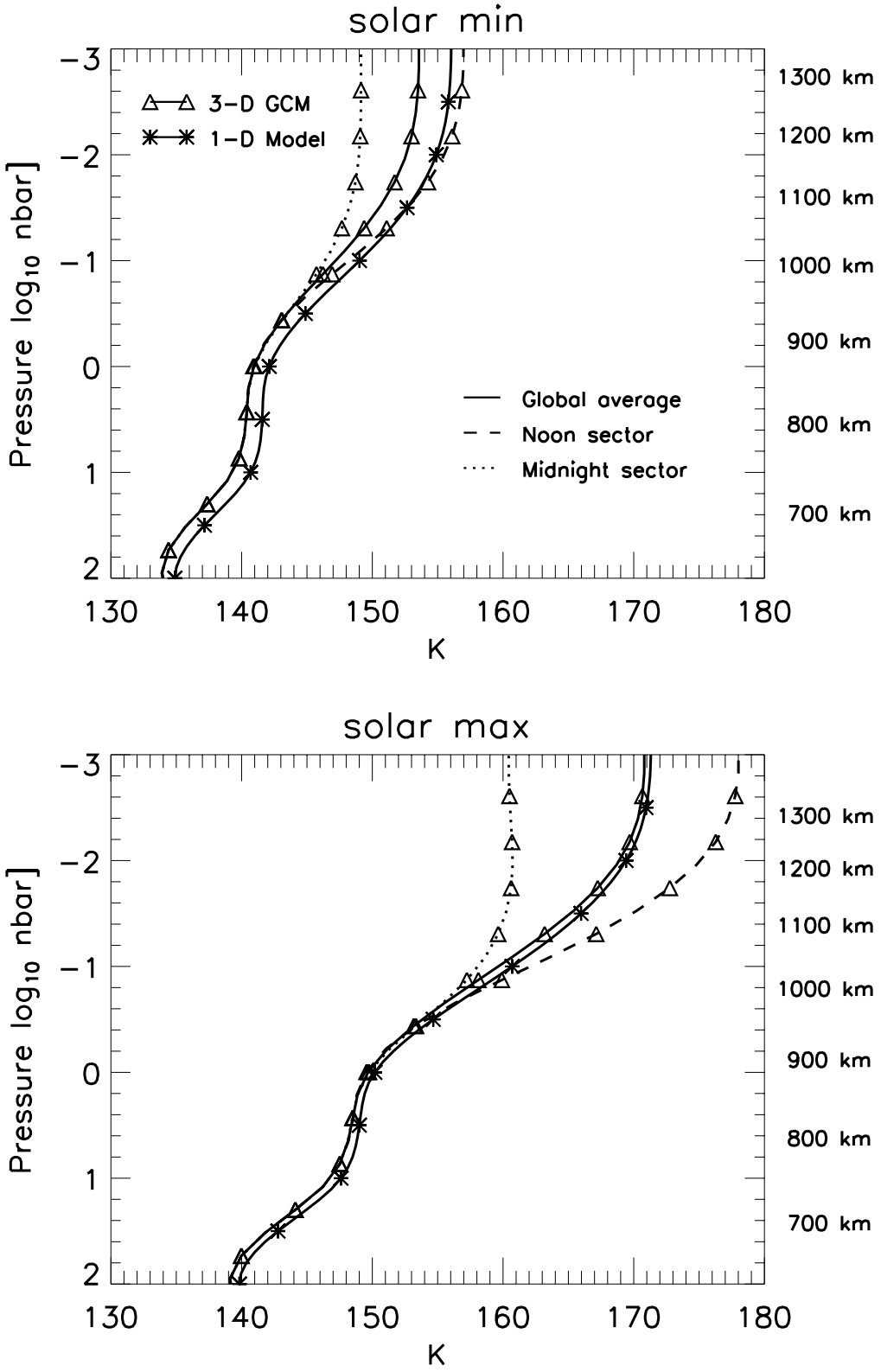
solar min
3-D GCM
1-D Model
Global average
Noon sector
Midnight sector
Pressure log10 nbar]
K
1300 km
1200 km
1100 km
1000 km
900 km
800 km
700 km
solar max
Pressure log10 nbar]
K

Fig.5

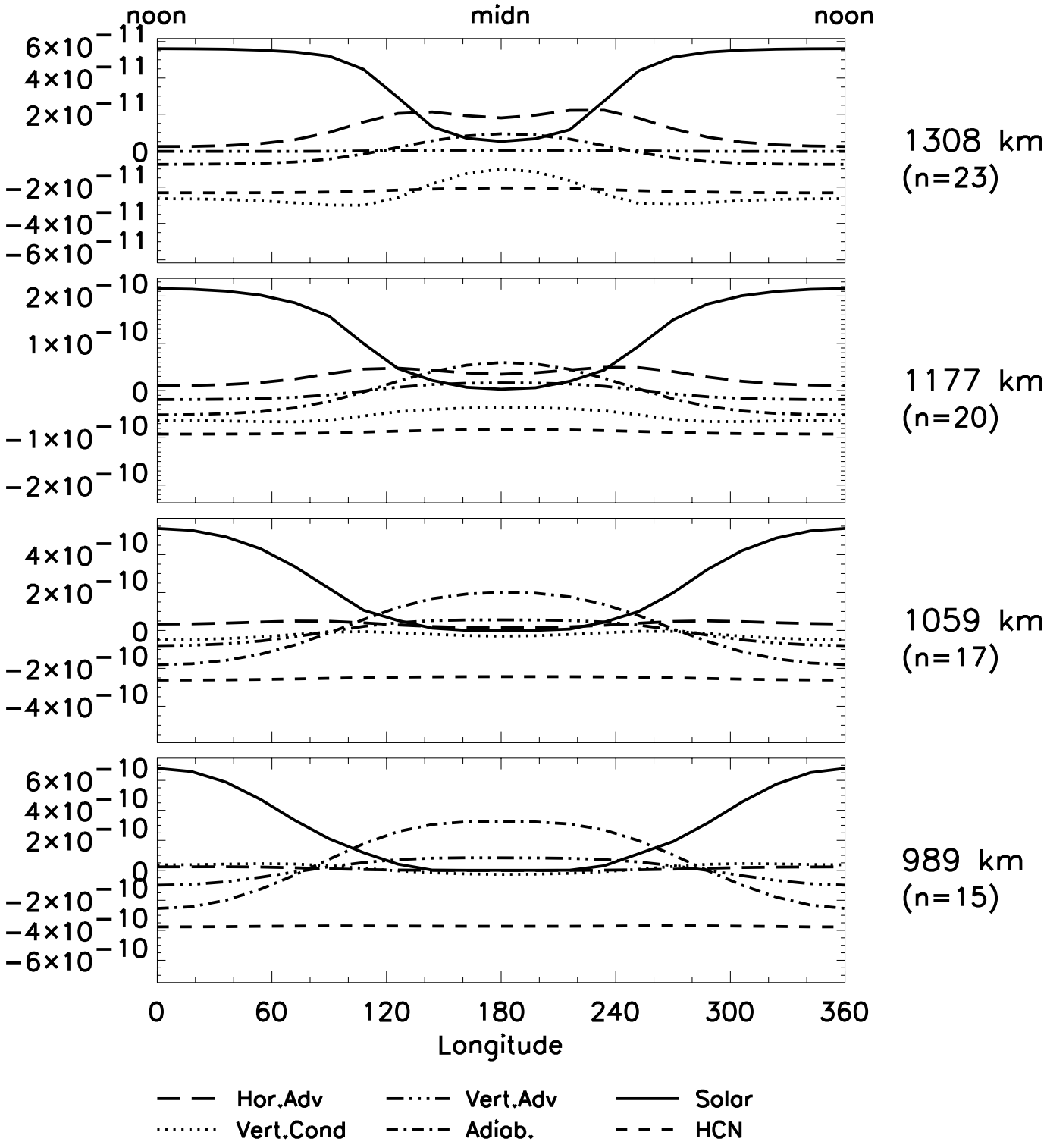
noon
midn
noon
6×10⁻¹¹
4×10⁻¹¹
2×10⁻¹¹
0
−2×10⁻¹¹
−4×10⁻¹¹
−6×10⁻¹¹
1308 km
(n=23)
2×10⁻¹⁰
1×10⁻¹⁰
0
−1×10⁻¹⁰
−2×10⁻¹⁰
1177 km
(n=20)
4×10⁻¹⁰
2×10⁻¹⁰
0
−2×10⁻¹⁰
−4×10⁻¹⁰
1059 km
(n=17)
6×10⁻¹⁰
4×10⁻¹⁰
2×10⁻¹⁰
0
−2×10⁻¹⁰
−4×10⁻¹⁰
−6×10⁻¹⁰
989 km
(n=15)
0
60
120
180
240
300
360
Longitude
Hor.Adv
Vert.Adv
Solar
Vert.Cond
Adiab.
HCN

Fig.6

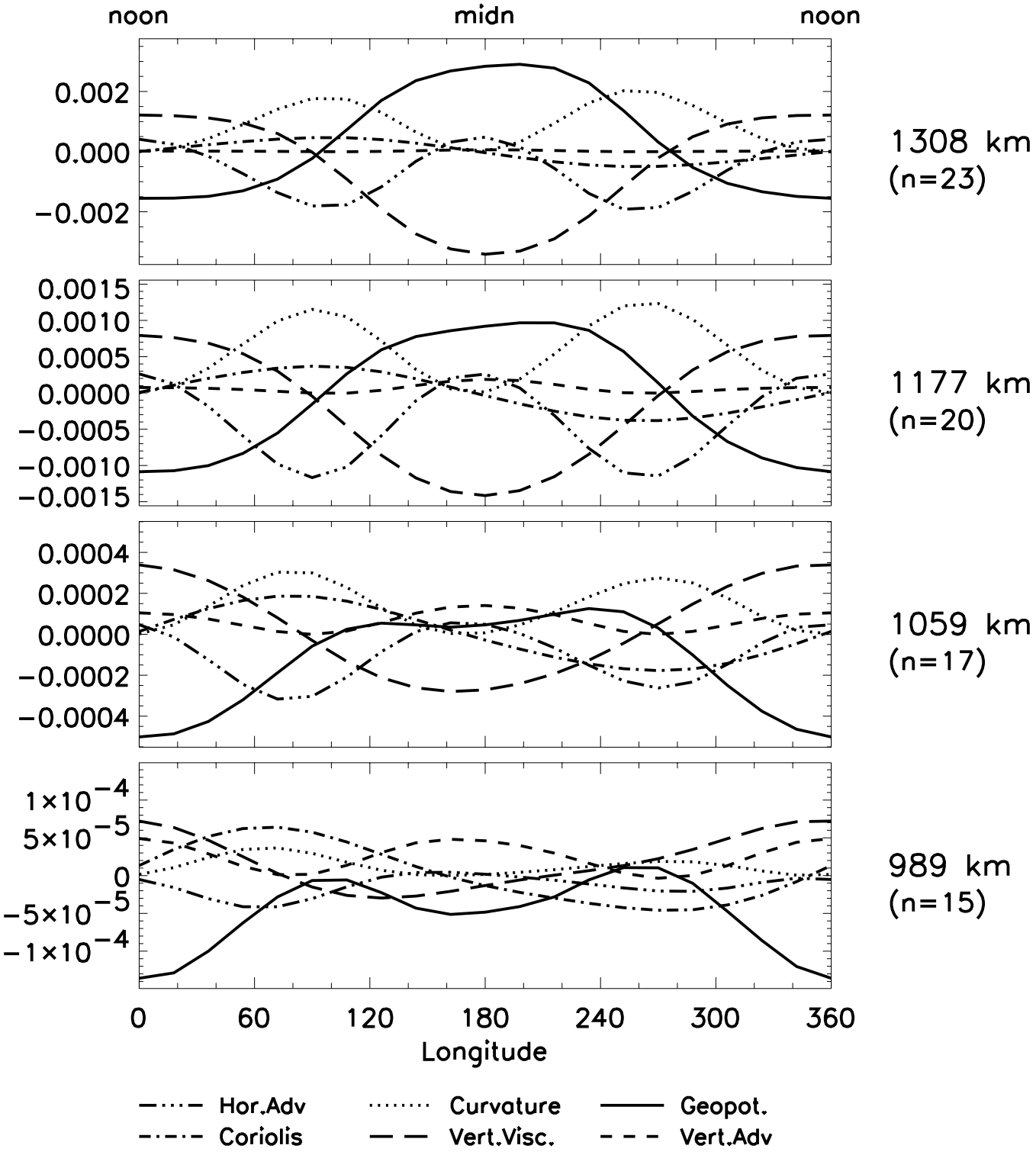
noon
midn
noon
0.002
0.000
−0.002
1308 km
(n=23)
0.0015
0.0010
0.0005
0.0000
−0.0005
−0.0010
−0.0015
1177 km
(n=20)
0.0004
0.0002
0.0000
−0.0002
−0.0004
1059 km
(n=17)
1×10−4
5×10−5
0
−5×10−5
−1×10−4
989 km
(n=15)
0
60
120
180
240
300
360
Longitude
Hor.Adv
Curvature
Geopot.
Coriolis
Vert.Visc.
Vert.Adv

Fig.7

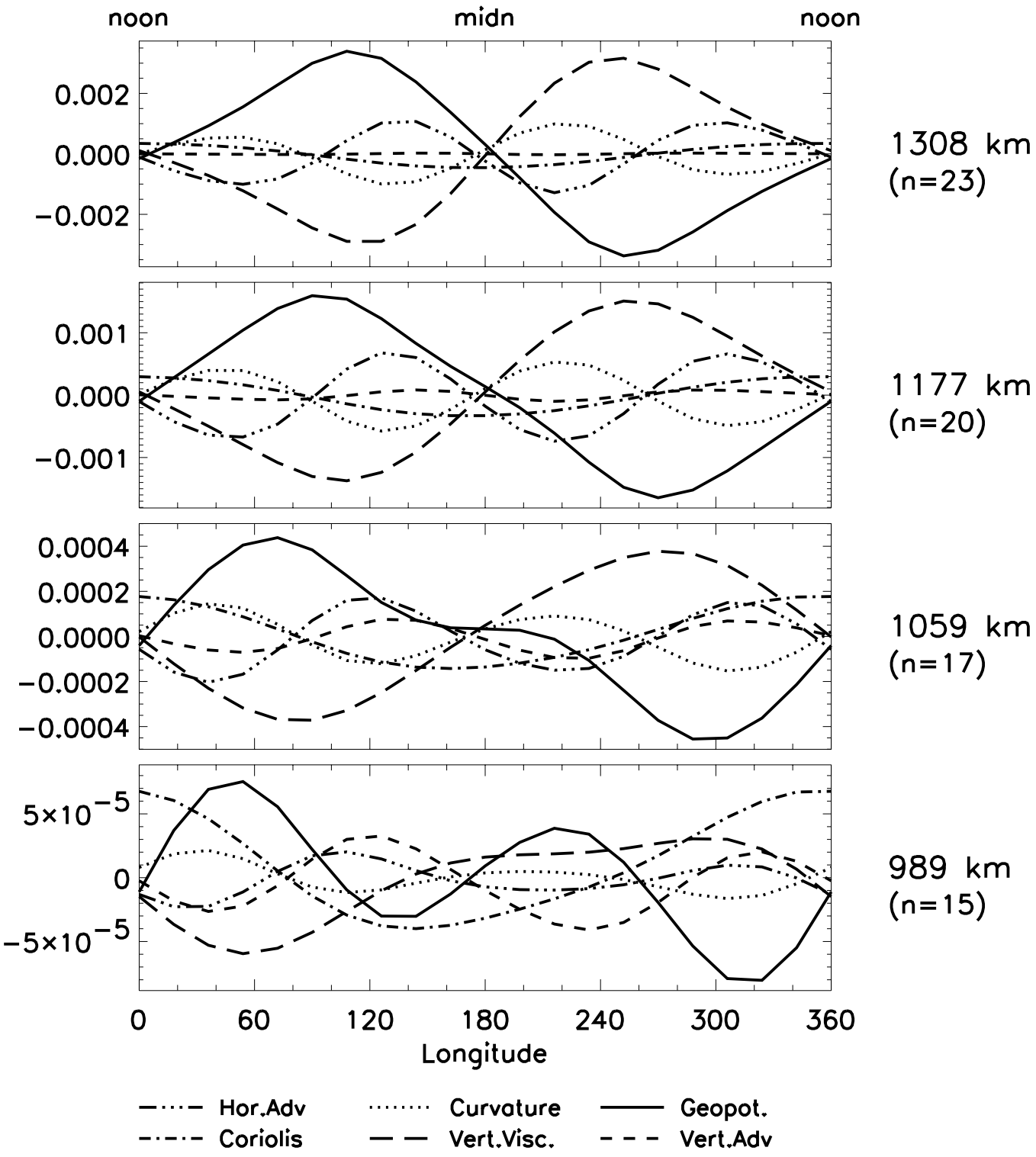
noon
midn
noon
0.002
0.000
−0.002
1308 km
(n=23)
0.001
0.000
−0.001
1177 km
(n=20)
0.0004
0.0002
0.0000
−0.0002
−0.0004
1059 km
(n=17)
5×10−5
0
−5×10−5
989 km
(n=15)
0
60
120
180
240
300
360
Longitude
Hor.Adv
Coriolis
Curvature
Vert.Visc.
Geopot.
Vert.Adv

Fig.8

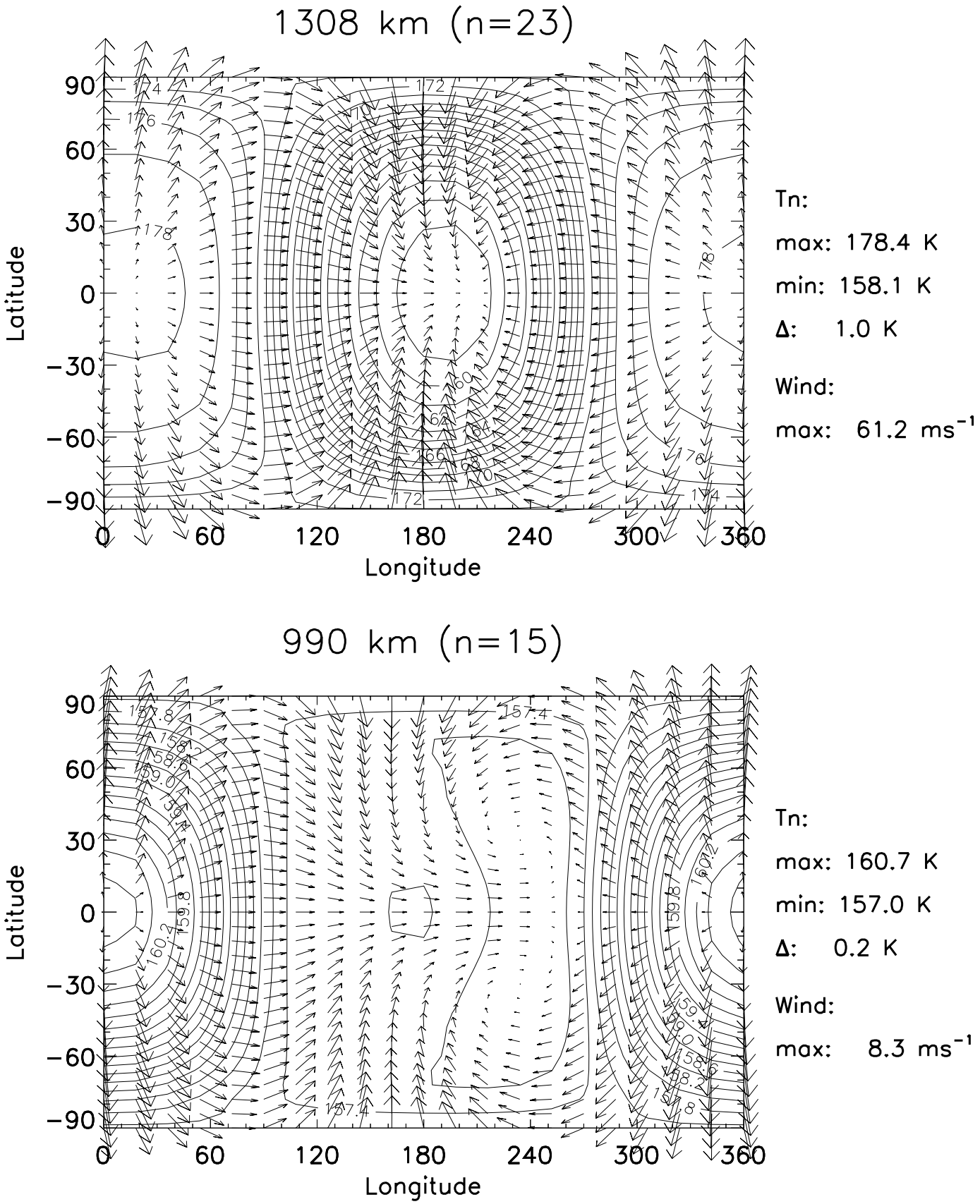
1308 km (n=23)
Latitude
Longitude
90
60
30
0
−30
−60
−90
0
60
120
180
240
300
360
Tn:
max: 178.4 K
min: 158.1 K
Δ: 1.0 K
Wind:
max: 61.2 ms⁻¹
990 km (n=15)
Latitude
Longitude
Tn:
max: 160.7 K
min: 157.0 K
Δ: 0.2 K
Wind:
max: 8.3 ms⁻¹

Fig.9

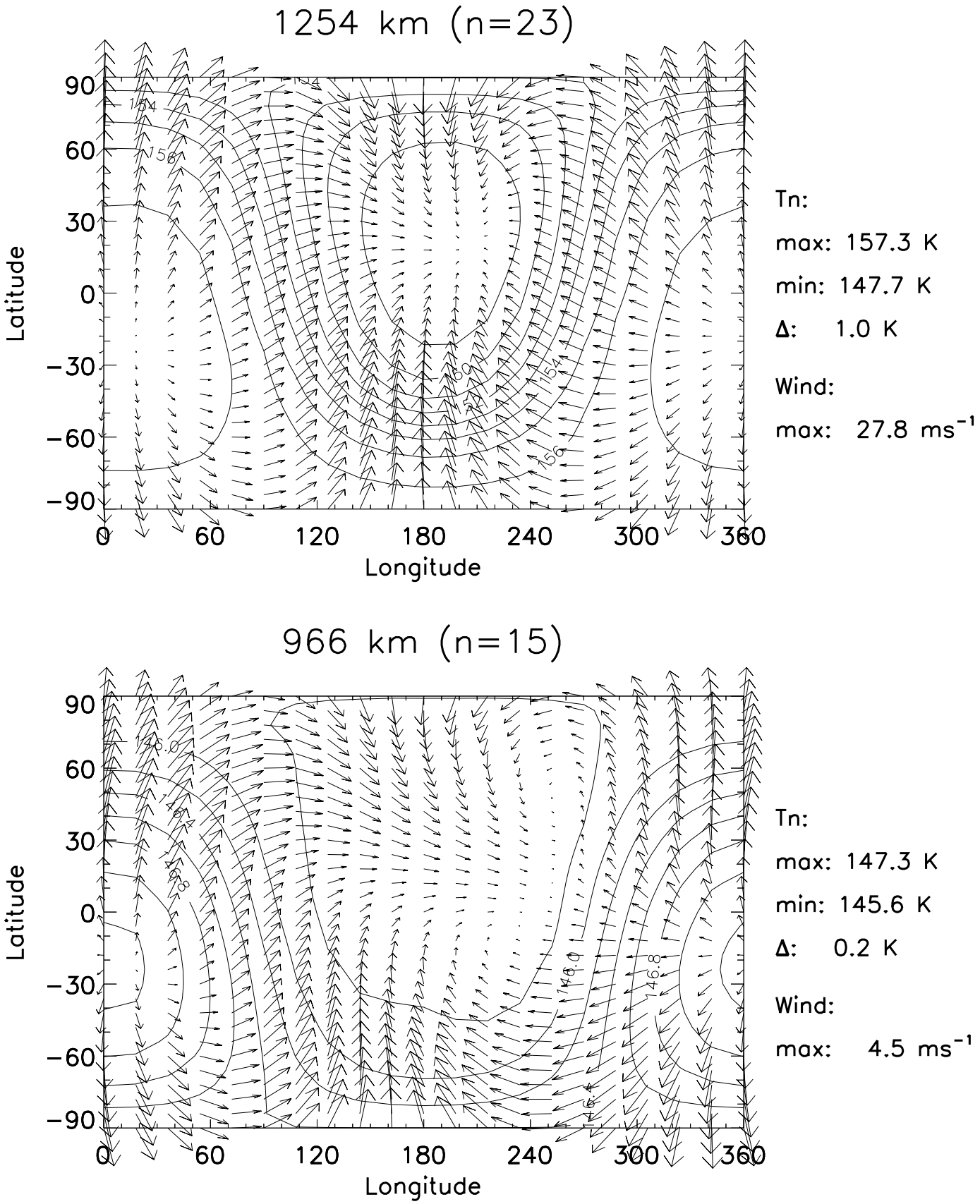
1254 km (n=23)
Latitude
Longitude
90
60
30
0
−30
−60
−90
0
60
120
180
240
300
360
154
156
158
160
152
Tn:
max: 157.3 K
min: 147.7 K
Δ: 1.0 K
Wind:
max: 27.8 ms⁻¹
966 km (n=15)
Latitude
Longitude
146.0
146.4
146.8
147.2
147.6
148.0
148.4
148.8
Tn:
max: 147.3 K
min: 145.6 K
Δ: 0.2 K
Wind:
max: 4.5 ms⁻¹

Fig.10

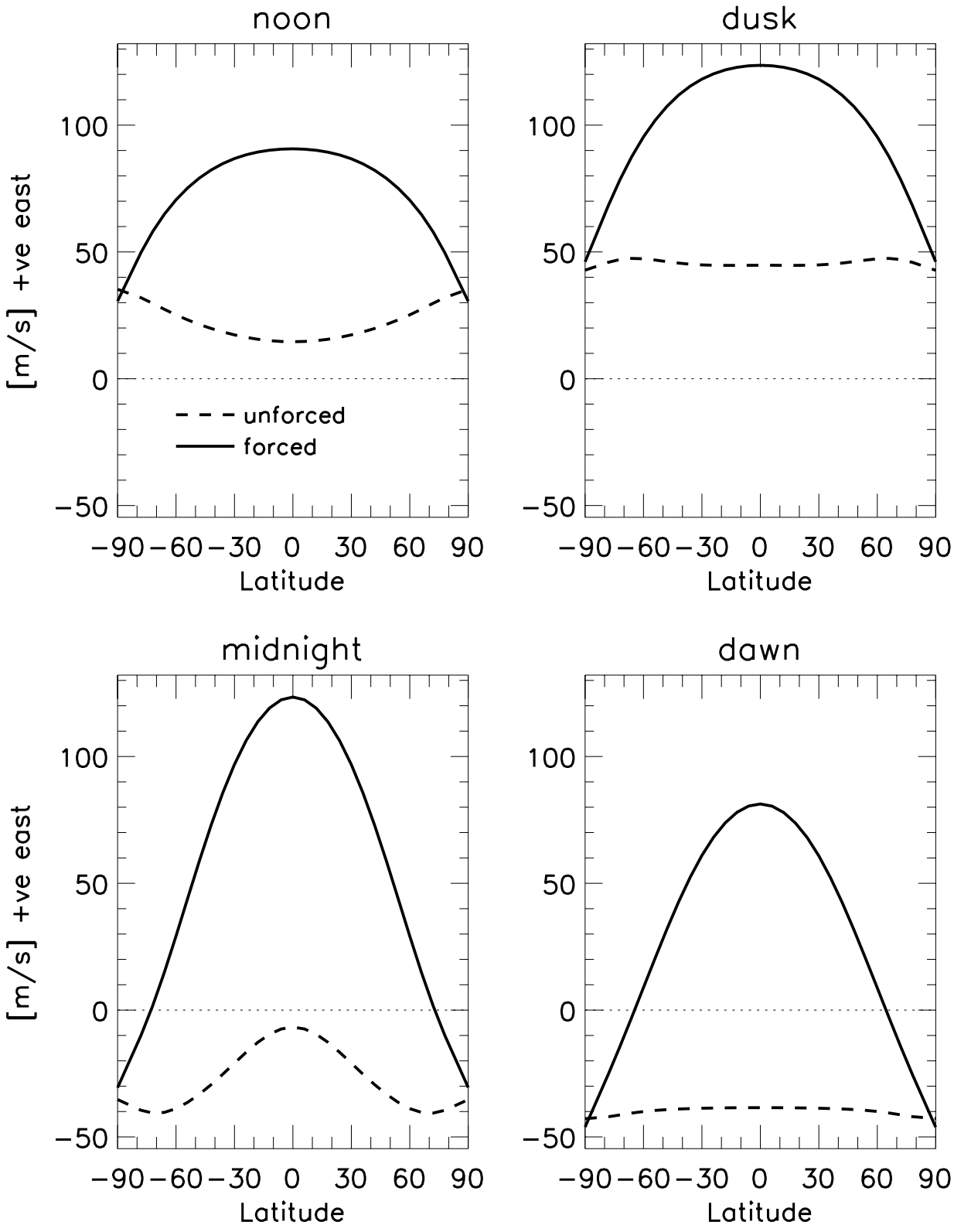
noon
dusk
midnight
dawn
[m/s] +ve east
100
50
0
−50
−90 −60 −30 0 30 60 90
Latitude
unforced
forced

Fig.11

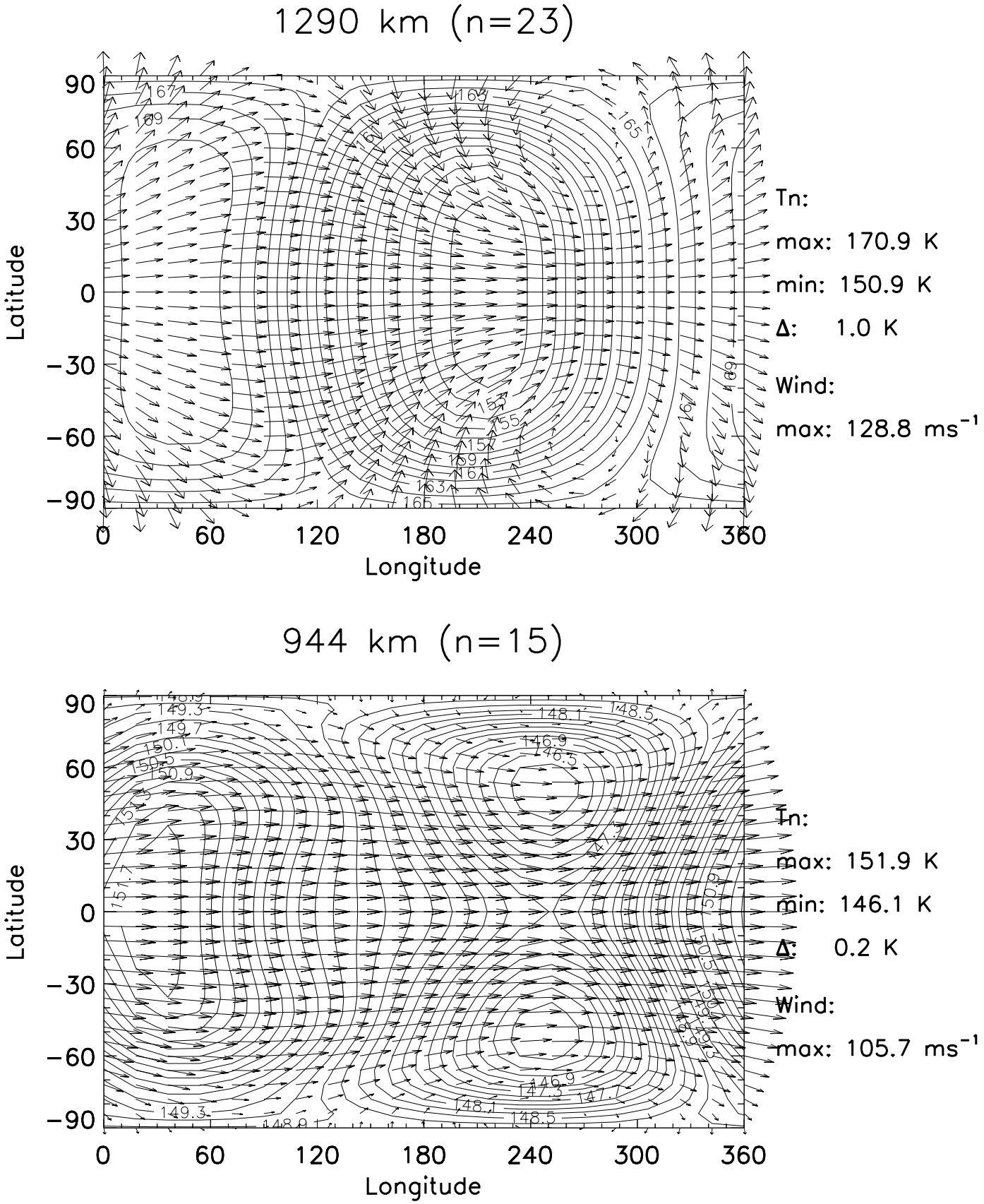
1290 km (n=23)
Latitude
Longitude
90
60
30
0
−30
−60
−90
0
60
120
180
240
300
360
Tn:
max: 170.9 K
min: 150.9 K
Δ: 1.0 K
Wind:
max: 128.8 ms⁻¹
944 km (n=15)
Latitude
Longitude
Tn:
max: 151.9 K
min: 146.1 K
Δ: 0.2 K
Wind:
max: 105.7 ms⁻¹